J. Fluid Mech. (1989), *vol.* 208, *pp.* 509–543
Printed in Great Britain

Growth of bioconvection patterns in a suspension of gyrotactic micro-organisms in a layer of finite depth

By N. A. HILL,[1] T. J. PEDLEY[1] AND J. O. KESSLER[2]

[1] Department of Applied Mathematics and Theoretical Physics, University of Cambridge, Silver Street, Cambridge CB3 9EW, UK

[2] Department of Physics, University of Arizona, Tucson, AZ 85721, USA

(Received 20 September 1988 and in revised form 5 May 1989)

The effect of gyrotaxis on the linear stability of a suspension of swimming, negatively buoyant micro-organisms is examined for a layer of finite depth. In the steady basic state there is no bulk fluid motion, and the upwards swimming of the cells is balanced by diffusion resulting from randomness in their shape, orientation and swimming behaviour. This leads to a bulk density stratification with denser fluid on top. The theory is based on the continuum model of Pedley, Hill & Kessler (1988), and employs both asymptotic and numerical analysis. The suspension is characterized by five dimensionless parameters: a Rayleigh number, a Schmidt number, a layer-depth parameter, a gyrotaxis number G, and a geometrical parameter measuring the ellipticity of the micro-organisms. For small values of G, the most unstable mode has a vanishing wavenumber, but for sufficiently large values of G, the predicted initial wavelength is finite, in agreement with experiments. The suspension becomes less stable as the layer depth is increased. Indeed, if the layer is sufficiently deep an initially homogeneous suspension is unstable, and the equilibrium state does not form. The theory of Pedley, Hill & Kessler (1988) for infinite depth is shown to be appropriate in that case. An unusual feature of the model is the existence of overstable or oscillatory modes which are driven by the gyrotactic response of the micro-organisms to the shear at the rigid boundaries of the layer. These modes occur at parameter values which could be realized in experiments.

1. Introduction

This paper is concerned with collective dynamical phenomena which occur when large numbers of small, self-propelled bodies are suspended in a fluid medium which is slightly less dense than they are. For example, in suspensions of certain species of swimming micro-organisms such as the alga *Chlamydomonas nivalis*. regions of increased concentration, coupled to bulk fluid motions are observed to arise spontaneously. This leads to convective instability (under the action of gravity) and hence to the establishment of convective patterns. The phenomenon is known as 'bioconvection'; it has some similarity with Rayleigh–Bénard convection, but originates solely from the swimming of the micro-organisms.

Pedley, Hill & Kessler (1988, hereinafter referred to as PHK) extended the theory of Childress, Levandowsky & Spiegel (1975, hereinafter referred to as CLS) (who analysed the bioconvective instability of a suspension of up-swimming cells) to develop a continuum model for a suspension of swimming, *gyrotactic* micro-

organisms. The centre of mass of such creatures is displaced from their centre of buoyancy so that in the absence of bulk fluid motions they tend to swim vertically upwards, a phenomenon known as 'negative geotaxis' (or 'gravitaxis'). However, when the bulk fluid motion has a horizontal component of vorticity, there is a tendency for the resultant viscous torque on a micro-organism to make it swim at a non-zero angle to the vertical. This behaviour was called 'gyrotaxis' by Kessler (1984). The orientation of such 'micro-swimmers' by torques due to gravity and fluid velocity gradients is not perfect. Neither are all the organisms identical, even in populations derived from a single parent cell. In this paper, as in its predecessors, we assume that such random deviations from perfect morphology, predictable swimming motions and purely deterministic behaviour can be described by a diffusive term incorporated into the equation representing conservation of cells. In bioconvection this diffusive component of the cells' motion is the analogue of thermal diffusion in Rayleigh–Bénard convection. We hope that it will eventually be possible to augment the assumption of the diffusion by more specific averages over cell properties, but a detailed knowledge of such cell properties is not yet available.

PHK gave an introduction to bioconvection and gyrotaxis and in a consideration of the linear stability of an initially uniform suspension in an unbounded layer, they found instability at finite wavenumbers, consistent with the formation of bioconvection patterns. However, their analysis is inappropriate for a shallow layer because the boundary conditions cannot be satisfied by a uniform suspension. The purpose of the present paper is to examine the linear stability of the steady, equilibrium state in a layer of *finite* depth using PHK's continuum model. The concentration of cells in the basic state increases exponentially with height so that the upward flux of cells due to negative geotaxis is balanced by a downward flux due to diffusion. A similar basic state and model were considered by CLS, but they did not include the effects of gyrotaxis and their model predicted a zero wavenumber at the onset of instability. Harashima, Watanabe & Fujishiro (1988) solved the nonlinear equations of the CLS model numerically in two dimensions for a layer of finite depth and width, and studied the evolution of bioconvection patterns from a uniform state. They found that the lengthscale of the initial instability is determined by the balance between up-swimming and diffusion in the basic state, but the scale of the later nonlinear convection patterns is determined by the overall layer depth.

The paper is organized as follows. The equations and boundary conditions of the continuum model are outlined in §2, and the steady equilibrium solution is given. In §3, the equations are non-dimensionalized, the dimensionless numbers describing the system are derived, and the equations are linearized about the equilibrium state. In §4, asymptotic expansions are used to find the neutral curve and growth rates, in certain limiting cases, and to predict critical wavelengths for the instability. The results of numerical calculation are presented in §5, and the application of this work to observations of bioconvection in suspensions of the motile alga, *C. nivalis*, is discussed in the final section.

2. The continuum model

As in PHK we assume a monodisperse cell population which can be modelled by a continuous distribution. Each cell has volume v and density $\rho+\Delta\rho$, where ρ is the (constant) density of the water in which the cells swim, and $\Delta\rho \ll \rho$. The number of cells in a small volume δV, centred at a point $\boldsymbol{x}^*$, is $n^*(\boldsymbol{x}^*, t^*)\delta V$, where $\boldsymbol{x}^*$ is measured relative to rectangular Cartesian axes $Ox^*y^*z^*$ with the z^*-axis vertically

up, and t^* is the time. The suspension is dilute so that $n^* v \ll 1$, and is taken to be incompressible. The continuum hypothesis is made. Thus, if $\boldsymbol{u}^*(\boldsymbol{x}^*, t^*)$ is the average velocity of all the material in δV, then incompressibility requires that

$$\nabla^* \cdot \boldsymbol{u}^* = 0. \tag{2.1}$$

The momentum equation, under the Boussinesq approximation and neglecting all effects of the cells except their negative buoyancy, is

$$\rho \frac{\mathrm{D}^* \boldsymbol{u}^*}{\mathrm{D}t^*} = -\nabla^* p_{\mathrm{e}}^* + n^* v \boldsymbol{g} \Delta\rho + \mu \nabla^{*2} \boldsymbol{u}^*, \tag{2.2}$$

where $p_{\mathrm{e}}^*(\boldsymbol{x}^*, t^*)$ is the excess pressure above the hydrostatic pressure, $\boldsymbol{g}$ is the acceleration due to gravity, and μ is the fixed dynamic viscosity of the suspension, which is taken to be approximately equal to that of water, since the suspension is dilute. $\mathrm{D}^*/\mathrm{D}t^* = \partial/\partial t^* + \boldsymbol{u}^* \cdot \nabla^*$ is the material time derivative.

Conservation of cells is expressed as

$$\frac{\partial n^*}{\partial t^*} = -\nabla \cdot \boldsymbol{j}^*, \tag{2.3}$$

where the flux of cells is

$$\boldsymbol{j}^* = n^* \boldsymbol{u} + n^* V_{\mathrm{c}} \boldsymbol{p} - D \nabla^* n^*. \tag{2.4}$$

The third term on the right-hand side of (2.4) represents the random component of cell locomotion. We assume that the diffusion coefficient D is scalar and independent of the other parameters in the problem. The second term in (2.4) arises from the swimming of the cells: $V_{\mathrm{c}} \boldsymbol{p}$ is the average swimming velocity relative to the fluid; V_{c} is assumed constant here and $\boldsymbol{p}(\boldsymbol{x}^*, t^*)$ is a unit vector representing the average orientation of cells in δV. The interaction between cells and fluid is inertia-free, and $\boldsymbol{p}(\boldsymbol{x}^*, t^*)$ can be calculated from the requirement that the viscous torque $\boldsymbol{L}$ exerted by the fluid on a cell in δV equals the torque due to gravity, namely

$$\boldsymbol{L} = -h\boldsymbol{p} \times \rho v \boldsymbol{g}, \tag{2.5}$$

where $-h\boldsymbol{p}$ is the displacement of the centre of mass from the centroid of a typical cell (see Pedley & Kessler 1987).

The vector $\boldsymbol{p}(\boldsymbol{x}^*, t^*)$ can be specified by Euler angles θ, ϕ referred to axes C123 through the geometric centre C of the cell and parallel to $Ox^*y^*z^*$:

$$\boldsymbol{p} = (\sin\theta\cos\phi, \sin\theta\sin\phi, \cos\theta). \tag{2.6}$$

The torque $\boldsymbol{L}$ on an ellipsoidal cell can be calculated from the vorticity $\boldsymbol{\omega}^*(\boldsymbol{x}^*, t)$ and the rate-of-strain tensor $e_{ij}^*(\boldsymbol{x}^*, t)$ in the flow at the location of the cell, using the theory of Jeffrey (1922) and others. Assuming the cell to be a prolate spheroid, with axis of symmetry parallel to $\boldsymbol{p}$, Pedley & Kessler (1987) show that (2.5) leads to the following equations for θ and ϕ:

$$B^{-1}\sin\theta = \omega_2^*\cos\phi - \omega_1^*\sin\phi + \alpha_0[\sin 2\theta(e_{11}^*\cos^2\phi + 2e_{12}^*\sin\phi\cos\phi + e_{22}^*\sin^2\phi - e_{33}) + 2\cos 2\theta(e_{13}^*\cos\phi + e_{23}^*\sin\phi)], \tag{2.7}$$

$$0 = -\omega_1^*\cos\theta\cos\phi - \omega_2^*\cos\theta\sin\phi + \omega_3^*\sin\theta + \alpha_0[\sin\theta(-e_{11}^*\sin 2\phi + 2e_{12}^*\cos 2\phi + e_{22}^*\sin 2\phi) + 2\cos\theta(-e_{13}^*\sin\phi + e_{23}^*\cos\phi)], \tag{2.8}$$

where

$$\alpha_0 = (a^2 - b^2)/(a^2 + b^2) \tag{2.9}$$

represents the cell's eccentricity, a and b being the semi-major and semi-minor axes. The constant B is the 'gyrotactic orientation parameter',

$$B = \mu\alpha_\perp/2h\rho g, \tag{2.10}$$

$\alpha_\perp$ being a dimensionless constant relating the viscous torque to the relative angular velocity of the cell. B has dimensions of time so that, if Ω is a typical velocity gradient in the flow, $B\Omega$ represents the ratio between viscous and gravitational torques on the cell. The angle θ between $\boldsymbol{p}$ and the vertical, for a spherical cell ($\alpha_0 = 0$) in a flow with only horizontal vorticity (Ω), is given by $\sin\theta = B\Omega$ (Kessler 1984; Pedley & Kessler 1987). Thus if $B = 0$, there is no gyrotaxis and the cells always swim vertically upwards; this is the limiting case considered by CLS. In the linear stability analysis presented here, fluid velocities are supposed to be sufficiently small that the torque $\boldsymbol{L}$ causes $\boldsymbol{p}$ to depart only a small amount from the vertical and there is no possibility of the cells tumbling (Kessler 1985).

The horizontal boundaries of the fluid layer are at $z^* = -H, 0$ and we assume that any sidewalls are sufficiently far away that the layer has effectively infinite width. Both free and rigid horizontal boundaries can be allowed for, but we shall concentrate on the case of two rigid boundaries. In experiments, there is usually a rigid lower boundary, and the upper boundary may be free or rigid. Indeed, even if the upper boundary is open to the air, algal cells often tend to collect at the surface forming what appears to be a packed layer, and it is unlikely that the boundary is ever fully stress-free, except immediately after vigorous mixing. In fact, if a coverslip is floated on the surface of such a suspension, forming a partial rigid upper boundary, the bioconvection patterns appear to be unaffected.

If $\hat{\boldsymbol{z}}$ is a unit vector in the z^*-direction, then the boundary conditions are

$$\boldsymbol{u}^* \cdot \hat{\boldsymbol{z}} = 0 \quad \text{on} \quad z^* = -H, 0 \tag{2.11}$$

and

$$\boldsymbol{j}^* \cdot \hat{\boldsymbol{z}} = 0 \quad \text{on} \quad z^* = -H, 0, \tag{2.12}$$

and for rigid boundaries

$$\boldsymbol{u}^* \times \hat{\boldsymbol{z}} = 0 \quad \text{on} \quad z = -H, 0, \tag{2.13}$$

while for a free boundary

$$\partial^2(\boldsymbol{u}^* \cdot \hat{\boldsymbol{z}})/\partial z^2 = 0. \tag{2.14}$$

The equations have a steady equilibrium solution

$$\boldsymbol{u}^* = 0, \quad \boldsymbol{p} = \hat{\boldsymbol{z}}, \quad n = N\exp(z^* V_c/D), \tag{2.15}$$

which satisfies all the boundary conditions. Here N is a normalization constant related to $\bar{n}$, the number of cells/unit volume for the whole layer, by

$$N = \bar{n}HV_c/D[1 - \exp(-HV_c/D)]. \tag{2.16}$$

Equation (2.15) is the basic state whose linear stability will be analysed; it is the same as that analysed by CLS, and we note that the depth scale for the cell, and hence density, accumulation that forms near the upper boundary $z^* = 0$ is

$$l = D/V_c. \tag{2.17}$$

The question of whether this basic state is ever achieved in experiments and how it is related to bioconvection is deferred to §6, at which point the analysis is sufficiently advanced for a proper quantitative discussion. Until then, we have in mind that after a suspension is initially well-mixed, any residual bulk fluid motions

are quickly damped out, so that the cells swim vertically up and the steady equilibrium given by (2.15) is formed. We are analysing this basic state to discover under what circumstances bioconvection will begin.

3. The linear stability problem

Before linearizing the governing equations about the equilibrium state (2.15), we make them dimensionless by scaling all lengths on H, the depth of the layer, time on the diffusive timescale H^2/D, and the bulk fluid velocity on D/H. The appropriate scaling for the pressure is $\nu D\rho/H^2$, and the cell concentration is scaled on N. Dimensionless variables are represented by unstarred symbols. The horizontal boundaries are at $z = -1, 0$. In terms of the new variables, the basic state (2.15) is

$$\boldsymbol{u} = 0, \quad \boldsymbol{p} = \hat{\boldsymbol{z}}, \quad n = \exp(dz), \tag{3.1}$$

where

$$d = HV_c/D \tag{3.2}$$

is the ratio of the cell swimming speed to the speed of bulk fluid motions. d can also be interpreted as the ratio of the layer depth H to the scale height l (see (2.17)) of the undisturbed concentration distribution, or the ratio of the diffusion time H^2/D to the up-swimming time H/V_c.

We now consider a small perturbation of amplitude ϵ ($0 < \epsilon \ll 1$) to the equilibrium state (3.1) so that

$$\boldsymbol{u} = \epsilon \boldsymbol{u}'(\boldsymbol{x}, t), \quad \boldsymbol{p} = \hat{\boldsymbol{z}} + \epsilon \boldsymbol{p}'(\boldsymbol{x}, t)$$

and

$$n = \exp(dz) + \epsilon n'(\boldsymbol{x}, t). \tag{3.3}$$

The components of $\boldsymbol{u}'$ are (u', v', w').

The dimensionless variables are substituted into the governing equations (2.1), (2.2) and (2.3), and linearized about the basic state to give at $O(\epsilon)$ the following problem for the perturbed quantities of (3.3):

$$\nabla \cdot \boldsymbol{u}' = 0, \tag{3.4}$$

$$S_c^{-1} \frac{\partial \boldsymbol{u}'}{\partial t} = -\nabla p_e - \left[\frac{Nvg\Delta\rho H^3}{\nu D\rho}\right] n' \hat{\boldsymbol{z}} + \nabla^2 \boldsymbol{u}' \tag{3.5}$$

and

$$\frac{\partial n'}{\partial t} + w' d \exp(dz) = -\nabla \cdot [d \exp(dz) \boldsymbol{p}' + dn' \hat{\boldsymbol{z}} - \nabla n'], \tag{3.6}$$

where

$$S_c = \nu/D$$

is the Schmidt number.

Similarly, the torque balance equations (2.7) and (2.8) are linearized, and $\boldsymbol{p}'$ is expressed in terms of $\boldsymbol{u}'$:

$$\boldsymbol{p}' = G[(1+\alpha_0)\, \partial \boldsymbol{u}_h'/\partial z - (1-\alpha_0)\, \nabla_h w'], \tag{3.7}$$

where the subscript h denotes the horizontal component and

$$G = BD/H^2 \tag{3.8}$$

is the dimensionless form of the gyrotactic orientation parameter B.

By elimination of p_e and $\boldsymbol{u}_h'$, (3.4)–(3.7) can be reduced to two equations for w' and n'. These quantities can then be decomposed into normal modes such that

$$w' = W(z) f(x, y) \exp(\sigma t), \quad n' = \Phi(z) f(x, y) \exp(\sigma t), \tag{3.9}$$

where the horizontal planform f satisfies

$$\nabla_{\mathrm{h}}^2 f = -k^2 f \tag{3.10}$$

for a constant (scaled) wavenumber $k = k^* H$, corresponding to a dimensionless wavelength $\lambda = 2\pi/k$. The governing equations become

$$\left(\frac{\sigma}{S_c} + k^2 - \frac{\mathrm{d}^2}{\mathrm{d}z^2}\right)\left(k^2 - \frac{\mathrm{d}^2}{\mathrm{d}z^2}\right) W = -\left[\frac{Nvg\Delta\rho H^3}{\nu D\rho}\right] k^2 \Phi \tag{3.11}$$

and

$$\left(\sigma + d\frac{\mathrm{d}}{\mathrm{d}z} + k^2 - \frac{\mathrm{d}^2}{\mathrm{d}z^2}\right)\Phi = d\exp(dz)\left[G(1+\alpha_0)\frac{\mathrm{d}^2}{\mathrm{d}z^2} - G(1-\alpha_0)\,k^2 - 1\right] W \tag{3.12}$$

subject to boundary conditions (for rigid boundaries)

$$W = \frac{\mathrm{d}\Phi}{\mathrm{d}z} - d\Phi = \frac{\mathrm{d}W}{\mathrm{d}z} = 0 \quad \text{at} \quad z = -1, 0. \tag{3.13}$$

At a free surface the last condition is replaced by

$$\frac{\mathrm{d}^2 W}{\mathrm{d}z^2} = 0. \tag{3.14}$$

The system of equations (3.11)–(3.14) is sixth order and has non-constant coefficients owing to the exponential variation of the equilibrium concentration. Equations (3.11) and (3.12) are akin to the equations for the vertical velocity and temperature in Bénard convection (Chandrasekhar 1961), and u', v' and p_{e} can be derived in the same manner as for Bénard convection, once w' and n' have been determined. Similar equations were derived by CLS. Our equations incorporate the effect of 'up-swimming' in the basic state, represented by the term $\mathrm{d}\Phi/\mathrm{d}z$ on the left-hand side of (3.12), which was included in CLS's work; the new effect of gyrotaxis is found in the terms containing a factor of G on the right-hand side of (3.12).

Equations (3.11) and (3.12) can be combined to give a single equation for W (or equally for Φ):

$$\left[\frac{\mathrm{d}^2}{\mathrm{d}z^2} - d\frac{\mathrm{d}}{\mathrm{d}z} - (k^2+\sigma)\right]\left[\frac{\mathrm{d}^2}{\mathrm{d}z^2} - \left(k^2 + \frac{\sigma}{S_c}\right)\right]\left[\frac{\mathrm{d}^2}{\mathrm{d}z^2} - k^2\right] W$$

$$= k^2 R \exp(dz)\left[G(1+\alpha_0)\frac{\mathrm{d}^2}{\mathrm{d}z^2} - G(1-\alpha_0)\,k^2 - 1\right] W, \tag{3.15}$$

where R is a Rayleigh number defined as

$$R = Nvg\,\Delta\rho H^3 d/\nu D\rho. \tag{3.16}$$

This particular choice of R is appropriate because it is the ratio of the buoyancy forces, which drive the bioconvection, to the viscous forces, which inhibit it, and is directly analogous to the usual Rayleigh number in thermal convection studies. It can also be thought of as the ratio of the diffusive time, H^2/D, in which cell accumulations are dispersed, to the time for such accumulations to sink a depth H in the viscous fluid.

It is also possible to scale length and velocity on l and $V_{\mathrm{c}}(=D/l)$ instead of H and D/H, giving an alternative definition of the Rayleigh number,

$$\hat{R} = Nvg\,\Delta\rho l^3/\nu D\rho,$$

and the gyrotaxis number, $\hat{G} = BD/l^2$.

This scaling has the advantage that $\hat{R}$ and $\hat{G}$ are independent of the layer depth H and are therefore constants for any particular suspension of micro-organisms of known concentration. The results are then straightforward to compare with experiments at different values of H. However, our choice of scales is more natural because we are interested in the macroscopic bioconvection patterns which are observed to extend over the whole depth of the layer so H, not l, is the expected lengthscale. Moreover, it turns out that our results are most clearly and simply expressed in terms of R and G given by (3.16) and (3.8).

3.1. *Stationary or oscillatory modes of instability*

The small perturbation (3.3) to the equilibrium state grows exponentially in time if $\gamma \equiv \mathrm{Re}\,(\sigma) > 0$ and decays if $\gamma < 0$. A neutral curve is defined as the locus of points in the (k,R)-plane on which $\gamma = 0$, but in general $\omega \equiv \mathrm{Im}\,(\sigma) \neq 0$, i.e. oscillatory (or overstable) solutions may exist. If $\omega = 0$ on a neutral curve, the corresponding instability is non-oscillatory, or stationary (sometimes called 'the principle of exchange of stabilities', Chandrasekhar 1961). This is the case for many systems where there is only one physical mechanism for instability, but it is often difficult to prove (see Drazin & Reid 1981). On the other hand, when there are two or more competing processes, overstability frequently occurs. This is the case for Bénard convection in a rotating frame or in the presence of a magnetic field (Chandrasekhar 1961).

In the Appendix, it is proved that the instability in our problem is stationary for the case of two stress-free boundaries, but the proof fails if at least one boundary is rigid, unless the gyrotaxis number G vanishes, in which case the instability is always stationary as shown by CLS. At first sight, there is no physical reason to anticipate oscillatory solutions when there is a rigid boundary, but numerical solution of (3.11)–(3.13) has revealed overstability. This surprising result is explained in §5 and is shown to depend on the shear due to the no-slip condition at a rigid boundary.

In our subsequent analysis, we determine for what values of R, G, S_c, α_0, d and k the basic state is neutrally stable ($\gamma = 0$). As discussed in §2, it is unlikely in an experiment that the upper surface of a suspension is ever fully stress-free, even if it is open to the air; therefore we concentrate on the case of two rigid horizontal boundaries from now on. The results are interpreted by plotting the neutral curves $R(k)$. In general, for given values in G, S_c, d, and α_0, there are an infinite number of branches $R^n(k)\,(n = 1,2,3,\ldots)$ of the neutral curve, corresponding to different solutions of the linear stability problem, of which the one of most interest is that on which R takes the smallest value, corresponding to the most unstable solution. Each solution may consist of one or more layers of convection cells stacked vertically above one another. A solution consisting of n layers is said to be *mode n*. Usually, but not always, the most unstable solution corresponds to the branch $R^1(k)$ of the neutral curve and is a mode 1 solution.

4. Asymptotic analysis

A number of limiting cases are analysed asymptotically in this section. The results are summarized in table 1 and figure 1. Full details of the analysis are available on request from the *JFM* Editorial Office, in an expanded version of this section. The exponential term in (3.12) makes it appropriate to consider two limits for asymptotic analysis. In the shallow-layer approximation $d \ll 1$, i.e. the layer depth H is much less than the lengthscale l of the equilibrium density distribution, and the exponential

$d \ll 1$		
$G = o(1)$	$\begin{cases} R^{(1)} = 720\left\{1+\frac{1}{2}d+\left(\frac{13}{105}+\frac{17\tilde{k}^2}{462}\right)d^2+\ldots\right\} \quad (4.20) \\ R^{(n)} = \omega_n^6/d^2\tilde{k}^2 \quad (n=2,3,\ldots) \quad (4.28) \end{cases}$	Case I Case II
$G \sim 1$	$\begin{cases} R^{(1)} = 720\{1+\frac{1}{2}d+d^2[\frac{13}{105}+G(1+\alpha_0)+\tilde{k}^2(\frac{17}{462}-\frac{2}{7}G(5-2\alpha_0))]+\ldots\} \quad (4.21) \\ R^{(n)} \sim d^{-2} \quad (n=2,3,\ldots) \quad \text{(analogous to Case II)} \end{cases}$	Case I Case III
$G \sim d^{-1}$	$\begin{cases} R^{(1)} = 720\{1+\frac{1}{2}d+d^2G[1+\alpha_0-2\tilde{k}^2(5-2\alpha_0)/7]+O(d^2)\} \quad (4.19) \\ R^{(n)} = \omega_n^4/d^2\tilde{k}^2G(1+\alpha_0)+\ldots \quad (n=2,3,\ldots) \quad (4.36) \end{cases}$	Case I Case IV
$G \sim d^{-2}$	$\begin{cases} R^{(1)} \to 720/[1-d^2G(1+\alpha_0)] \quad \text{as} \quad \tilde{k} \to 0 \ (d^2G(1+\alpha_0) < 1) \\ R^{(n)} = \omega_n^4/d^2\tilde{k}^2G(1+\alpha_0)+\ldots \quad (n=1,2,\ldots) \quad (4.36) \\ R^{(1)} \text{ is stationary when } d^2G(1+\alpha_0) < 1; \\ R^{(1)} \text{ is oscillatory at small values of } \tilde{k} \text{ otherwise.} \end{cases}$	Case IV
$G \geqslant O(d^{-3})$	$\begin{cases} R^{(n)} = \omega_n^4/d^2\tilde{k}^2G(1+\alpha_0)+\ldots \quad (n=1,2,\ldots) \quad (4.36) \\ R^{(1)} \text{ is oscillatory at small values of } \tilde{k}. \end{cases}$	Case IV
$d \gg 1$		
$d^2G(1+\alpha_0) < 1$	$R^{(1)} = \dfrac{2d^4}{1-d^2G(1+\alpha_0)}\left\{1+\dfrac{4}{d}\dfrac{k(\sinh k\cosh k-k)}{\sinh^2 k-k^2}+O(d^{-2})\right\}$	(4.45)

TABLE 1. Summary of the results of the asymptotic analysis of neutral curves $R^{(n)}(k)$ for the limiting cases considered in §4. When $d \ll 1$, the equations for the neutral curves are given for small wavenumbers $k = d\tilde{k} \sim d$, as a function of the order of the magnitude of G; for the deep layer, $d \gg 1$, the equations for the neutral curves are given for values of $k = O(1)$.

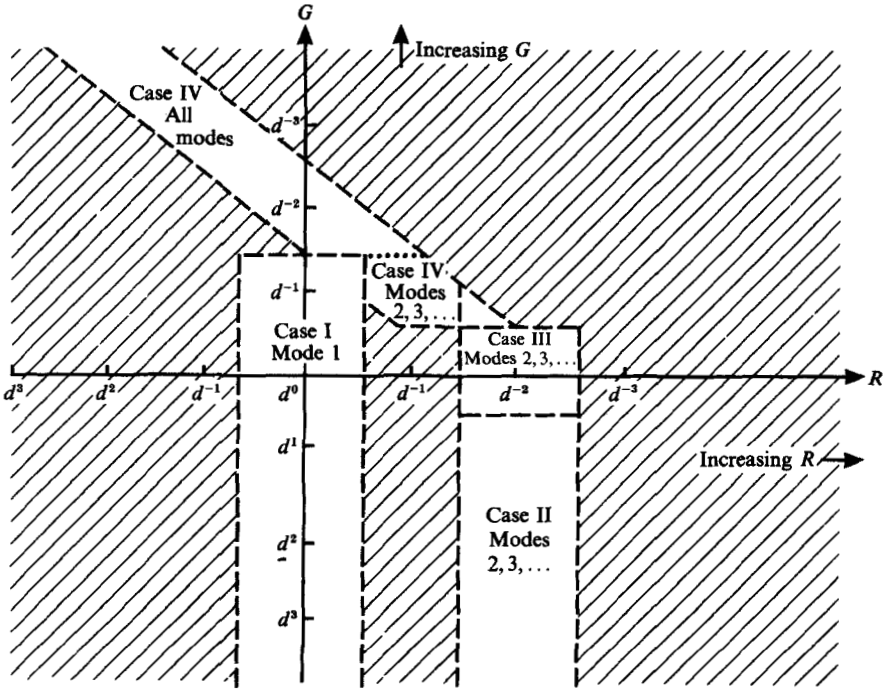

FIGURE 1. Regions of $(\log_d R, \log_d G)$-space covered by solutions near the neutral curves in the four cases of §4.1, for the shallow layer $d \ll 1$, and for small wavenumbers $\tilde{k} = k/d = O(1)$.

term is approximately linear, with consequent simplification. For a deep layer, d is large and, in the basic state, the cells are concentrated in a boundary layer at the upper surface, so that the method of matched asymptotic expansions can be used.

The purpose of the subsequent asymptotic analysis is to give insight into the fluid mechanics of bioconvection and to provide checks on the numerical solutions of §5. Wherever possible the growth rate, σ, is taken to be complex and non-zero, but in many cases the analysis becomes so complicated that it is necessary to resort to numerical solutions of transcendental equations, which offer little analytical insight. In such cases attention is confined to the neutral curves on which $\mathrm{Re}(\sigma) = 0$. Moreover, for all the parameter values considered analytically below, the numerical solution shows that $\mathrm{Im}(\sigma)$ vanishes, i.e. there are only stationary solutions. Attempts at asymptotic solutions for other parameter values lead to such complications that the numerical solutions of §5 are preferred; such parameter values do sometimes exhibit oscillatory instability. Of course, in applying this linear stability theory to experiments in §6, we shall need to determine the critical Rayleigh number, R_c, and wavenumber, k_c, at which each neutral curve has its minimum. Then, we expect the theory to describe the flow only for values of R close to R_c, and we shall compare the wavenumber of observed pattern spacing with that of the predicted wavenumber, k_c.

4.1. *Shallow-layer approximation*, $0 < d \ll 1$

Rather than solving (3.15) in the shallow-layer approximation, it is more convenient to consider (3.11) and (3.12), which we rewrite as

$$\left(\frac{\mathrm{d}^2}{\mathrm{d}z^2} - d^2\tilde{k}^2 - \frac{\sigma}{S_c}\right)\left(\frac{\mathrm{d}^2}{\mathrm{d}z^2} - d^2\tilde{k}^2\right) W = -dR\tilde{k}^2\Phi, \tag{4.1}$$

and

$$\left(\frac{\mathrm{d}^2}{\mathrm{d}z^2} - d\frac{\mathrm{d}}{\mathrm{d}z} - d^2\tilde{k}^2 - \sigma\right)\Phi = d(1 + dz + \tfrac{1}{2}d^2z^2 + \ldots)\left[1 - G(1+\alpha_0)\frac{\mathrm{d}^2}{\mathrm{d}z^2} + d^2\tilde{k}^2 G(1-\alpha_0)\right] W, \tag{4.2}$$

where

$$\tilde{k} = k/d. \tag{4.3}$$

The leading-order versions of (4.1) and (4.2) can be solved in principle by elementary methods. However, once the boundary conditions are applied, the solution for the neutral curve $R(k; G, \alpha_0)$ leads to a transcendental equation, which has to be solved numerically. Instead, we choose to simplify (4.1) and (4.2) further to gain a better understanding of the analysis and to obtain results which can be compared with the numerical solution of the full linear stability problem in §5 below. Therefore we first consider small wavenumbers where $k \sim d$ and so

$$\tilde{k} \sim 1. \tag{4.4}$$

This is equivalent to scaling k^* on l^{-1} rather than H^{-1}, and corresponds to a horizontal planform of wavelength $\lambda^* \sim l$, much greater than the layer depth H.

We now concentrate on the analysis of neutral curves and examine the possible balances between the terms in (4.1) and (4.2) which indicate the relevant asymptotic expansions. For non-vanishing solutions, which satisfy the six leading-order boundary conditions

$$\frac{\mathrm{d}\Phi}{\mathrm{d}z} = W = \frac{\mathrm{d}W}{\mathrm{d}z} = 0 \quad \text{at} \quad z = -1, 0, \tag{4.5}$$

the highest-order derivatives in (4.1) and (4.2) must be retained at leading order. It is also readily shown that in each of the cases discussed below the leading-order balance in (4.1) must give

$$\left(\frac{\mathrm{d}^2}{\mathrm{d}z^2}-\frac{\sigma}{S_c}\right)\frac{\mathrm{d}^2W}{\mathrm{d}z^2}=-dR\tilde{k}^2\Phi, \tag{4.6}$$

otherwise there is only the trivial solution. Physically, (4.5) represents the balance between the viscous term $\mathrm{d}^4W/\mathrm{d}z^4$ and the buoyancy force on the right-hand side which drives the flow. Without loss of generality, we also specify that

$$\Phi = O(1). \tag{4.7}$$

There are then four possible leading-order balances between the terms in (4.2) which are shown below, together with the appropriate leading-order versions of (4.2), which we recall is derived from the cell conservation equation (2.3), when $\sigma = 0$.

Case I:

$$G \leqslant O(d^{-1}), \quad R \sim 1, \quad \frac{\mathrm{d}^2\Phi}{\mathrm{d}z^2}=0.$$

Case II:

$$G \leqslant O(d), \quad R \sim d^{-2}, \quad \frac{\mathrm{d}^2\Phi}{\mathrm{d}z^2}=dW.$$

Case III:

$$G \sim 1, \quad R \sim d^{-2}, \quad \frac{\mathrm{d}^2\Phi}{\mathrm{d}z^2}=d\left[W-G(1+\alpha_0)\frac{\mathrm{d}^2W}{\mathrm{d}z^2}\right].$$

Case IV:

$$R \leqslant O(d^{-1}), \quad RG \sim d^{-2}, \quad \frac{\mathrm{d}^2\Phi}{\mathrm{d}z^2}=-dG(1+\alpha_0)\frac{\mathrm{d}^2W}{\mathrm{d}z^2}.$$

The regions of (R, G) parameter space covered by these cases are illustrated in figure 1. In Case I, the leading-order balance in (4.2) is purely diffusive; we shall show below that there is a second-order balance between diffusion and the swimming of the micro-organisms. In Case II, the leading-order balance is between diffusion and advection of the micro-organisms by the bulk fluid flow, while the balance also includes gyrotaxis due to vertical shear in the flow in Case III. Finally, in Case IV, diffusion balances the gyrotactic term alone. We shall restrict attention to Cases I, II and IV, although mathematically II is a special case of III, because once again the latter leads to a complicated transcendental eigenvalue problem which itself requires numerical solution.

4.1.1. *Case I*: $k \sim d$ *and* $G \leqslant O(d^{-1}), R \sim 1$

Consistent with (4.7), we choose

$$\Phi \sim 1, \quad R \sim 1, \quad G \sim d^{-1}, \quad W \sim d$$

and expand Φ, R and W in powers of d, so that

$$\Phi = \sum_{n=0}^{\infty} d^n \Phi_n, \quad W = \sum_{n=1}^{\infty} d^n W_n, \quad R = \sum_{n=0}^{\infty} d^n R_n, \tag{4.8}$$

and we write

$$G = d^{-1}G_{-1} \quad (G_{-1} = O(1)). \tag{4.9}$$

To obtain information about the growth rate in this particular case, we allow σ to be non-zero and, since it turns out that $\sigma \sim d^2$, we expand it as

$$\sigma = \sum_{n=2}^{\infty} d^n \sigma_n \tag{4.10}$$

a priori, for convenience. On substituting (4.8), (4.9) and (4.10) into (4.1) and (4.2) and the boundary conditions (3.13), we find at leading order that

$$\frac{\mathrm{d}^4 W_1}{\mathrm{d}z^4} + \tilde{k}^2 R_0 \Phi_0 = 0, \quad \frac{\mathrm{d}^2 \Phi_0}{\mathrm{d}z^2} = 0, \tag{4.11a, b}$$

and

$$\frac{\mathrm{d}\Phi_0}{\mathrm{d}z} = W_1 = \frac{\mathrm{d}W_1}{\mathrm{d}z} = 0 \quad \text{at} \quad z = -1, 0, \tag{4.11c}$$

while at second order

$$\frac{\mathrm{d}^4 W_2}{\mathrm{d}z^4} + \tilde{k}^2 R_0 \Phi_1 = -\tilde{k}^2 R_1 \Phi_0, \tag{4.12a}$$

$$\frac{\mathrm{d}^2 \Phi_1}{\mathrm{d}z^2} = \frac{\mathrm{d}\Phi_0}{\mathrm{d}z} - G_{-1}(1+\alpha_0)\frac{\mathrm{d}^2 W_0}{\mathrm{d}z^2}, \tag{4.12b}$$

with boundary conditions

$$\frac{\mathrm{d}\Phi_1}{\mathrm{d}z} - \Phi_0 = W_2 = \frac{\mathrm{d}W_2}{\mathrm{d}z} = 0 \quad \text{at} \quad z = -1, 0. \tag{4.12c}$$

The second- and higher-order systems of equations are inhomogeneous and must satisfy solvability conditions. These conditions are found in the usual manner (Ince 1956): each system of inhomogeneous equations is multiplied by the adjoint of the homogeneous system and integrated from $z = -1$ to 0, and the resulting integral must vanish. This is equivalent to setting to zero the integral of the cell conservation equation (4.2) over the layer depth.

The solvability condition at $O(d)$ is satisfied identically, independently of σ_2 and R_0, while at $O(d^2)$

$$(\tilde{k}^2 + \sigma_2)\int_{-1}^{0} \Phi_0 \,\mathrm{d}z + \int_{-1}^{0} W_1 \,\mathrm{d}z = 0, \tag{4.13}$$

and at $O(d^3)$

$$(\tilde{k}^2 + \sigma_2)\int_{-1}^{0} \Phi_1 \,\mathrm{d}z + \int_{-1}^{0} W_2 \,\mathrm{d}z$$

$$= G_{-1}[1 + \alpha_0 - (1-\alpha_0)\tilde{k}^2]\int_{-1}^{0} W_1 \,\mathrm{d}z - \sigma_3 \int_{-1}^{0} \Phi_0 \,\mathrm{d}z - \int_{-1}^{0} z W_1 \,\mathrm{d}z. \tag{4.14}$$

The leading-order solution is

$$\Phi_0 = 1, \quad W_1 = -\tfrac{1}{24} R_0 \tilde{k}^2 (z^4 + 2z^3 + z^2), \tag{4.15}$$

where Φ_0 has been normalized without loss of generality. Imposing the solvability condition (4.13) gives

$$\sigma_2 = \tilde{k}^2 \left(\frac{R_0}{720} - 1\right). \tag{4.16}$$

The second-order solution is

$$\left.\begin{aligned} \Phi_1 &= z - G_{-1}(1-\alpha_0)\,W_1, \\ W_2 &= \left(\frac{\tilde{k}^2 R_0}{40} - \frac{\tilde{k}^2 R_1}{12} - G_{-1}(1+\alpha_0)\frac{\tilde{k}^4 R_0^2}{360}\right) z^3 + \left(\frac{\tilde{k}^2 R_0}{60} - \frac{\tilde{k}^2 R_1}{24} - G_{-1}(1+\alpha_0)\frac{\tilde{k}^4 R_0^2}{560}\right) z^2 \\ &\quad - \frac{\tilde{k}^2 R_0}{120} z^5 - \frac{\tilde{k}^2 R_1 z^4}{24} - G_{-1}(1+\alpha_0)\frac{\tilde{k}^4 R_0^2}{720}\left(\frac{z^8}{56} + \frac{z^7}{14} + \frac{z^6}{12}\right), \end{aligned}\right\} \tag{4.17}$$

and the solvability condition (4.14) yields

$$\sigma_3 = \frac{\tilde{k}^2 R_1}{720} - \frac{\tilde{k}^2 R_0}{720}\left[\tfrac{1}{2} + G_{-1}(1+\alpha_0)\right] + \frac{\tilde{k}^4 R_0}{720} G_{-1}\left[1 - \alpha_0 + \frac{3R_0}{720}\frac{(1+\alpha_0)}{7}\right]. \tag{4.18}$$

Thus, with this choice of scaling, there is just one solution, the vertical structure of which consists of one bioconvection cell and which we therefore class as mode 1. On the neutral curve $\sigma = 0$ and then

$$R = 720\{1 + d[\tfrac{1}{2} + G_{-1}(1+\alpha_0) - 2\tilde{k}^2 G_{-1}(5-2\alpha_0)/7]\} + O(d^2). \tag{4.19}$$

Proceeding to the next order, it can be shown that, when $G = 0$, the neutral curve is

$$R = 720\left\{1 + \tfrac{1}{2}d + \left(\frac{13}{105} + \frac{17\tilde{k}^2}{462}\right)d^2\right\} + O(d^3). \tag{4.20}$$

Thus, in the absence of gyrotaxis, $k = 0$ is a local minimum of the neutral curve and the wavelength of the most unstable mode is infinite (as found by CLS). On the other hand, in the presence of gyrotaxis (4.19) shows that $k = 0$ is a local maximum, since $\alpha_0 < 1$, from which it follows that the most unstable mode must occur at some value of $k > O(d)$, as suggested by observations (e.g. Kessler 1985). Examples of the neutral curves are given in figure 2(*a*) (see §5) when $d = 0.1$, $G = 0, 0.5$ and $\alpha_0 = 0.2$.

The critical value of G at which $k = 0$ changes from being a minimum to a local maximum of the neutral curve can be found by noting that, if $G = O(1)$, then linearity shows that

$$R = 720\{1 + \tfrac{1}{2}d + d^2[\tfrac{13}{105} + G(1+\alpha_0) + \tilde{k}^2(\tfrac{17}{462} - \tfrac{2}{7}G(5-2\alpha_0))]\} + O(d^3) \tag{4.21}$$

and the critical value of G is

$$G_c = \frac{17}{132(5-2\alpha_0)} + O(d). \tag{4.22}$$

Estimates of σ for fixed values of R can be obtained from (4.16) and (4.18), which provide a useful check on numerical calculations, and in particular we note that gyrotaxis introduces a dependence on $\tilde{k}^4$.

The preceding analysis is readily shown to be valid in the limit as $k \to 0$, but not for values of $k \gg O(d)$. However, it can be extended to the general case when $d, k \ll 1$ by expanding in powers of both d and k^2, which gives

$$R = 720\left[1 + \tfrac{1}{2}d + k^2\left(\frac{17}{462} - \frac{2G}{7}(5-2\alpha_0)\right)\right] + O(d^2, dk^2, k^4) \tag{4.23}$$

on the neutral curve (cf. (4.21)). A special case of this result occurs when

$$d^{\frac{1}{2}} \ll k \ll 1 \tag{4.24}$$

and the expansion proceeds in powers of k^2. This is the scheme used by CLS, but their analysis was not strictly valid because k was allowed to tend to zero without regard to the restriction (4.24). Instead, (4.23) shows that

$$R \to 720 \quad \text{as} \quad d, k^2 \to 0.$$

The neutral curves given by (4.19), (4.20), (4.21) and (4.23) all show that $k = 0$ is a minimum of the neutral curve when $G < G_c$, and that R decreases monotonically as k increases when $G > G_c$, provided that d and $k \ll 1$. Thus, up to the accuracy of the expansion schemes, we conclude that the most unstable wavenumber is $k_c = 0$ when $G < G_c$, and $k_c \geqslant O(1)$ when $G > G_c$.

The inequalities which define Case I do not specify the scaling uniquely, even when restrictions (4.6) and (4.7) are imposed. However, a little analysis shows that the only possible scalings for non-trivial solutions are

$$\Phi \sim 1, \quad R \sim 1, \quad W \sim d, \quad G \leqslant O(d^{-1}) \tag{4.25}$$

and so there are no other fundamentally different solutions.

4.1.2. *Case II*: $k \sim d$ *and* $G \leqslant O(d), R \sim d^{-2}$.

We suppose that $\sigma = 0$,

$$\Phi \sim 1, \quad G \sim d, \quad R \sim d^{-2}, \quad W \sim d^{-1}, \tag{4.26}$$

and expand the variables in powers of d in a similar fashion to the analysis for Case I. The leading-order solution is found to be

$$W = d^{-1}\{A\cos(\omega z) + B\sin(\omega z) + \exp(\tfrac{1}{2}\omega z\sqrt{3})[C\cos(\tfrac{1}{2}\omega z) + D\sin(\tfrac{1}{2}\omega z)] + \exp(-\tfrac{1}{2}\omega z\sqrt{3})[E\cos(\tfrac{1}{2}\omega z) + F\sin(\tfrac{1}{2}\omega z)]\} + O(1), \tag{4.27}$$

where

$$\omega^6 = d^2 R\tilde{k}^2. \tag{4.28}$$

A, B, C, D, E and F are constants determined by applying the boundary conditions, and for a non-trivial solution it can be shown that ω takes values

$$\omega_2 = 2\pi, \quad \omega_3 \approx 3\pi, \quad \omega_4 = 4\pi, \quad \omega_5 \approx 5\pi, \ldots.$$

At this point, we have multiple solutions to the linear stability problem. Corresponding to the roots $\omega_2, \omega_3, \ldots$, there are branches of the neutral curve $R^{(2)}(k)$, $R^{(3)}(k), \ldots$ given by (4.28). We must also examine the structure of the vertical velocity field $W(z)$ to determine the mode or type of solution. A solution is said to be *mode n* if $W(z)$ changes sign $(n-1)$ times for $-1 < z < 0$. In other words mode $N (n = 1, 2, \ldots)$ consists of n layers of convection cells stacked vertically one above the other throughout $-1 < z < 0$ (see §3).

The neutral curve of the smallest root ω_2 is given by (4.28) as

$$R^{(2)} = 2\pi^6/d^2\tilde{k}^2 + O(d^{-1}) \approx 6.15 \times 10^4/d^2\tilde{k}^2 + O(d^{-1}),$$

and the constants $A, \ldots, F$ can be calculated for this branch to show that

$$W \propto d^{-1}\sin\pi z[\sinh(\pi\sqrt{3})\cos(\pi z) - \cosh(\tfrac{1}{2}\pi\sqrt{3})\sinh(\pi[z+\tfrac{1}{2}]\sqrt{3})],$$

which is antisymmetric about $z = -\frac{1}{2}$ and is therefore mode 2.

In Case II, the only alternatives to the choice of scales (4.26), which are consistent with (4.6) and (4.7), are of the form

$$\Phi \sim 1, \quad R \sim d^{-2}, \quad W \sim d^{-1}, \quad G \sim d^m \quad (m = 2, 3, \ldots).$$

Since G does not appear in the leading-order problem, the alternative choices of scaling in which G is of smaller magnitude will not change the nature of the leading-order solution, but just make refinements at higher orders.

In order to interpret the results of Cases I and II, we suppose without loss of generality that (4.7) holds and ask what solutions are possible for a given value of G. It is clear that for $G \leqslant O(d)$, Cases I and II both provide solutions. Case I gives the $R^{(1)}$ branch corresponding to mode 1, and Case II provides the higher branches and modes. This is summarized in figure 1 and at the top of table 1. Also, when $G \sim 1$, Cases I and III both provide solutions. Although, as mentioned previously, Case III has not been completely analysed analytically, it is reasonable to expect that again Case I gives the $R^{(1)}$ branch and Case III gives the higher branches $R^{(n)} \sim d^{-2}$.

4.1.3. *Case IV*: $k \sim d$ *and* $R \leqslant O(d^{-1}), RG \sim d^{-2}$

As in Case I, we analyse the shallow-layer approximation to the governing equations in the limit of small wavenumbers. Because of the complicated nature of the eigenvalue problem which arises here, we exclude the possibility of oscillatory solutions on the neutral curves, in the more detailed calculations, by setting $\sigma = 0$. Possible scalings are of the form

$$\Phi \sim G, \quad G \sim d^{-m}, \quad R \sim d^{m-2}, \quad W \sim d^{m-1} \quad (m = 1, 2, \ldots), \tag{4.29}$$

and the problem subdivides naturally into the three cases $m = 1$, $m = 2$ and $m \geqslant 3$. When $m = 1, G \sim d^{-1}$ and we have already demonstrated that Case I provides a mode-1 solution when $G \sim d^{-1}$. Thus we might anticipate that the new scaling yields the higher-order modes by analogy with Case II. Moreover, when $m \geqslant 2$, we shall show that Case IV gives all the solution branches, including the mode-1 solution. What is more unexpected is that when $m = 2$ and G exceeds a critical value, the solution for the lowest branch breaks down at small wavenumbers. We conjecture that in this case oscillatory solutions exist and we shall indicate an appropriate scaling for such solutions.

We begin by setting $m = 2$ and define

$$\Phi = \sum_{0}^{\infty} d^n \Phi_n, \quad W = \sum_{1}^{\infty} d^n W_n, \quad R = \sum_{0}^{\infty} d^n R_n, \quad G = d^{-2} G_{-2}, \tag{4.30}$$

which is consistent with (4.6) and (4.7). Expressions (4.30) are substituted into (4.1), (4.2) and (3.13), and at leading order

$$\frac{\mathrm{d}^4 W_1}{\mathrm{d}z^4} + \tilde{k}^2 R_0 \Phi_0 = 0, \quad \frac{\mathrm{d}^2}{\mathrm{d}z^2}[\Phi_0 + G_{-2}(1+\alpha_0) W_1] = 0$$

subject to the boundary conditions

$$\frac{\mathrm{d}\Phi_0}{\mathrm{d}z} = W_1 = \frac{\mathrm{d}W_1}{\mathrm{d}z} = 0 \quad \text{on} \quad z = -1, 0.$$

This system of equations has the solution

$$\left.\begin{aligned} \phi_0 &= G_{-2}(1+\alpha_0)(K - W_1), \\ W_1 &= A\cos\omega z + B\sin\omega z - (A+K)\cosh\omega z - B\sinh\omega z + K, \end{aligned}\right\} \tag{4.31}$$

where

$$\omega^4 = \tilde{k}^2 R_0 G_{-2}(1+\alpha_0)$$

and A, B and K are constants which satisfy

$$\begin{pmatrix} \cos\omega-\cosh\omega & \sinh\omega-\sin\omega \\ \sinh\omega+\sin\omega & \cos\omega-\cosh\omega \end{pmatrix}\begin{pmatrix} A \\ B \end{pmatrix} = K\begin{pmatrix} \cosh\omega-1 \\ -\sinh\omega \end{pmatrix}. \tag{4.32}$$

This equation can in principle be solved (for $A/K, B/K$) for any value of ω save that for which the matrix on the left-hand side is singular, in which case $K = 0$.

The boundary conditions on Φ_0 to this order are degenerate and we proceed to the next order, $O(d)$, to find an additional constraint on Φ_0 arising from the solvability condition. Similarly, there is an additional constraint on Φ_1 at $O(d^2)$, and so on to higher orders. As in Case I, the solvability condition is found by integrating the cell conservation equation over the layer depth. It turns out that the solvability condition is satisfied identically at $O(d)$, but at $O(d^2)$ it is easily shown that

$$\int_{-1}^{0} W_1 \,\mathrm{d}z = -F(\tilde{k}; G_{-2}, \alpha_0) K, \tag{4.33}$$

where

$$F(\tilde{k}; G_{-2}, \alpha_0) = \frac{G_{-2}(1+\alpha_0)\tilde{k}^2}{1+G_{-2}(1-\alpha_0)\tilde{k}^2 - G_{-2}(1+\alpha_0)(\tilde{k}^2+1)},$$

using the leading-order solution (4.31). Evaluating the integral in (4.33) and incorporating (4.32), the conditions on A, B and K can be written as

$$\begin{pmatrix} \cos\omega-\cosh\omega & \sinh\omega-\sin\omega & 1-\cosh\omega \\ \sinh\omega+\sin\omega & \cos\omega-\cosh\omega & \sinh\omega \\ \sin\omega-\sinh\omega & \cos\omega+\cosh\omega-2 & \omega-\sinh\omega+F \end{pmatrix}\begin{pmatrix} A \\ B \\ K \end{pmatrix} = 0, \tag{4.34}$$

which is an eigenvalue problem for ω, and hence for R. Equation (4.34) has a non-trivial solution if and only if

$$\omega(1+F)(1-\cos\omega\cosh\omega) = 2[\sinh\omega(1-\cos\omega)+\sin\omega(1-\cosh\omega)]. \tag{4.35}$$

There is a set of even roots of (4.35), associated with even modes, given by

$$\omega_{2m'} \approx \tfrac{1}{2}(4m'+1)\pi \quad (m' = 1, 2, \ldots)$$

independently of the value of F. The odd roots do depend on F and, when

$$G_{-2}(1+\alpha_0) < 1,$$

there is also a set of odd roots with associated odd modes such that

$$0 \leqslant \omega_1 \leqslant \omega_2 \leqslant \omega_3 \leqslant \ldots.$$

The most unstable branch is

$$R^{(1)} = \omega_1^4/k^2 G(1+\alpha_0) + O(d) \tag{4.36}$$

and mode 1 is the preferred mode. When $\tilde{k} \gg 1, \omega_1 \approx \frac{3}{2}\pi$ and therefore $R^{(1)} \propto k^{-2}$ so that disturbances of shorter wavelengths are more unstable than those of longer wavelengths. The behaviour of $R^{(1)}$ as $\tilde{k} \to 0$ can be calculated by expanding (4.35) in a Taylor series about $\omega = 0$ which shows that

$$R^{(1)} \to \frac{720}{1-G_{-2}(1+\alpha_0)} \quad \text{as} \quad \tilde{k} \to 0. \tag{4.37}$$

The roots $\omega_n (n > 1)$ do not tend to 0 as $\tilde{k}$ tends to 0, so

$$R^{(n)} \sim \tilde{k}^{-2} \to \infty \quad \text{as} \quad \tilde{k} \to 0 \quad \text{for} \quad n > 1. \tag{4.38}$$

When (4.38) is compared with (4.19) and (4.21), we see that the effect on the neutral curve of increasing the value of G, from $O(d^{-1})$ to $O(d^{-2})$, is to increase the value of $R^{(1)}(0)$ from 720 until $R^{(1)}(0)$ tends to ∞ as G tends to $1/d^2(1+\alpha_0)$.

Hurle, Jakeman & Pike (1967) considered the Bénard problem with boundaries of finite conductivity and were able to show that, in the limit of perfectly insulating boundaries, the Rayleigh number of the lowest, odd mode tends to 720 as the wavenumber tends to zero, and the Rayleigh number of the first even mode tends to ∞ as the wavenumber tends to zero. Thus the unusual contrast between the behaviour of $R^{(1)}$ given by (4.37) and that of the higher branches given by (4.38) has a parallel in Benard convection. Indeed this comparison was noted by CLS but, when gyrotaxis is included in the analysis, $\tilde{k} = 0$ is a local *maximum* of the neutral curve $R^{(1)}$ both in this case (which we shall demonstrate later numerically) and in Case I, whereas CLS, and Hurle *et al.* (1967), found that $\tilde{k} = 0$ was in all cases a local *minimum*.

It can be shown that there is a critical value of $F, F_c \approx -0.75$, such that the root ω_1 does not exist when $F_c < F < 0$. When $G_{-2}(1+\alpha_0)$, F always lies outside $(-1, 0)$, but when $G_{-2}(1+\alpha_0) > 1$ and $\tilde{k}$ is sufficiently small, $F_c < F < 0$ and the branch $R^{(1)}$ corresponding to mode 1 does not exist.

We now consider the other possible scalings given by (4.29), and the analysis hinges on the solvability condition (4.33). It is readily seen that when $m = 1$, and the variables are expanded in powers of d accordingly, solvability requires simply that

$$\int_{-1}^{0} W_0 \, dz = 0,$$

while if $m \geqslant 3$, the solvability condition becomes

$$\int_{-1}^{0} W_{m-1} \, dz = \frac{(1+\alpha_0)\,\tilde{k}^2 K}{(1+\alpha_0)+2\alpha_0\,\tilde{k}^2}.$$

Suppose firstly, that $m = 1$: the analysis proceeds as before, when $m = 2$, but with F now set to zero, and we conclude that ω_1 does not exist for any values of $\tilde{k}$, i.e. the most unstable mode when $m = 1$ is mode 2.

Now suppose that $m \geqslant 3$ and set

$$F = -\tilde{k}^2/(1+\alpha'\tilde{k}^2), \quad \alpha' = 2\alpha_0/(1+\alpha_0)$$

in the earlier analysis. F is independent of G and takes values in the interval $(-1/\alpha', 0)$. α' takes values between 0 and 1, so that $-1/\alpha' \leqslant -1$, and therefore ω_1 exists only for values of $\tilde{k}^2 \gtrsim 0.75/(1-0.75\alpha') > 0$. So when $m \geqslant 3$, mode 1 is found only for sufficiently large values of $\tilde{k}$.

Once again, when $G = O(d^{-1})$ (and $m = 1$), Case I provides the most unstable branch, $R^{(1)}$ (see figure 1 and table 1). However, when $G \geqslant O(d^{-2})$, Case I is no longer valid and there is no other scaling that would lead to a *stationary* branch giving mode 1 as the most unstable mode, and we must therefore seek oscillatory solutions. This conclusion is supported by the fact that numerical investigations, when $d \ll 1$ and $\tilde{k} = O(1)$, have found overstability when $d^2G(1+\alpha_0) > 1$ (see §5); it should be noted that this quantity is independent of H, and therefore depends only on the properties of the organism and of the suspending fluid. If, in addition to the relations (4.30), we assume that $\sigma = O(1)$, it is possible to outline an asymptotic solution which should lead to oscillatory modes. However, the resulting eigenvalue problem is so complicated as to require full numerical solution.

Cell radius	a	10^{-3} cm
Cell volume	v	5×10^{-10} cm^3
Cell density ratio	$\Delta\rho/\rho$	5×10^{-2}
Cell diffusivity	D	5×10^{-4} cm^2 s^{-1}
Gyrotaxis number	G	$0.5/d^2$
Cell eccentricity	α_0	0.2
Swimming speed	V_c	10^{-2} cm s^{-1}
Mean concentration	$\bar{n}$	10^6 cm^{-3}
Kinematic viscosity	ν	10^{-2} cm^2 s^{-1}
Schmidt number	S_c	20
Sublayer depth	l	0.05 cm

TABLE 2. Estimates of typical parameters for a suspension of the alga *Chlamydomonas nivalis*. The gyrotaxis number $G = BD/H^2$ is the dimensionless form of the gyrotactic orientation parameter B defined in (2.10), where H is the layer depth. d is the scaled depth H/l where the sublayer depth $l = D/V_c$.

Finally we note that, for suspensions of *C. nivalis*,

$$d^2G(1+\alpha_0) \approx 0.6$$

(see table 2), so that overstability is unlikely to be found in such a suspension but, as discussed later, it is possible that overstability could be found in suspensions of different species of micro-organisms.

We conclude the shallow-layer analysis with the following observations. For small wavenumbers, $k \sim d$, and when $G = O(1)$, mode 1 is the most unstable mode and the neutral curve has a local minimum at $k = 0$. As G increases to $O(d^{-1})$, $k = 0$ becomes a local maximum. It can also be shown that $R^{(1)} \sim k^2$ as $k \to \infty$ when $G = O(d^{-1})$, so that $R^{(1)}$ must have a global minimum when $k \geqslant O(1)$. This leads to a prediction of a critical wavelength for instability which is finite. Finally, for large values of $G \geqslant O(d^{-2})$, oscillatory modes are found.

4.2. *Deep-layer approximation*, $d \gg 1$

When $d \gg 1$ the exponential profile of the equilibrium solution gives a boundary layer at the upper surface containing a high concentration of cells. Variables are therefore expanded in inverse powers of d and the method of matched asymptotic expansions is used to resolve the boundary layer. From (3.12) and (3.13), we expect Φ to be exponentially small in the outer region, away from the upper boundary layer, where $z = O(1)$. The numerical results of §5 suggest that for oscillatory solutions, which are found for certain parameter values, $\mathrm{Im}\,(\sigma) = O(d^2)$ and should therefore be found in the leading-order terms of the asymptotic analysis in the boundary layer. However, attempts at a suitable scaling to achieve such a balance have been unsuccessful, as we describe below. Thus the following analysis is restricted to cases where $\sigma = O(1)$, in which case it is shown that σ is always real. For clarity, we first consider neutral curves, on which $\mathrm{Re}\,(\sigma) = 0$, and suppose that $\mathrm{Im}\,(\sigma) = 0$ also.

When $d \gg 1$, the governing linear stability equations (3.11)–(3.13) in the outer region become

$$\Phi = 0, \quad \left(\frac{\mathrm{d}^2}{\mathrm{d}z^2} - k^2\right)^2 W(z) = 0 \tag{4.39}$$

subject to boundary conditions

$$W = \frac{\mathrm{d}W}{\mathrm{d}z} = 0 \quad \text{as} \quad z = -1 \tag{4.40}$$

and matching conditions as $z \to 0$. The general solution of (4.39) and (4.40) is

$$W = -kA(z+1)\cosh[k(z+1)] + [A + B(z+1)]\sinh[k(z+1)],$$

where constants A and B can be expanded in powers of d, e.g.

$$A = A_0 + d^{-1}A_{-1} + d^{-2}A_{-2} + \ldots.$$

In the inner region, define

$$z_I = dz = O(1), \quad \mathrm{D}_I \equiv \frac{\mathrm{d}}{\mathrm{d}z_I},$$

in terms of which the equations become

$$(\mathrm{D}_I^2 - d^{-2}k^2)^2 W = -d^{-5}Rk^2\Phi, \tag{4.41a}$$

$$(\mathrm{D}_I^2 - \mathrm{D}_I - d^{-2}k^2)\,\Phi = -d\exp(z_I)[G(1+\alpha_0)\,\mathrm{D}_I^2 - G(1-\alpha_0)\,d^{-2}k^2 - d^{-2}]\,W \tag{4.41b}$$

and

$$(\mathrm{D}_I - 1)\,\Phi = W = \mathrm{D}_I W = 0 \quad \text{at} \quad z_I = 0 \tag{4.41c}$$

with matching conditions as $z_I \to -\infty$. As in the shallow-layer approximation, there are several balances possible between the terms in (4.41) but the presence of the exponential term in (4.41*b*) makes the analysis more difficult and we restrict attention to the case when

$$G \leqslant O(d^{-2}), \quad W \sim d^{-1} \quad \text{as} \quad d \to \infty$$

which covers the parameter range of interest in experiments, as will be discussed later (see also table 2). In particular we define

$$W = \sum_{1}^{\infty} d^{-n}W_{-n}, \quad \Phi = \sum_{0}^{\infty} d^{-n}\Phi_{-n}, \quad R = \sum_{-4}^{\infty} d^{-n}R_{-n}, \quad G = d^{-2}G_{-2}, \tag{4.42}$$

where $\Phi \sim 1$ as in (4.7). Again for buoyancy to drive the flow the magnitude of the right-hand side of (4.41*a*) must balance the largest term on the left-hand side.

Substituting the expansions (4.42) into (4.41) gives at leading order

$$\mathrm{D}_I^4 W_{-1} + R_4 k^2 \Phi_0 = 0, \quad \mathrm{D}_I(\mathrm{D}_I - 1)\,\Phi_0 = 0,$$

and at second order

$$\mathrm{D}_I^4 W_{-2} + R_4 k^2 \Phi_{-1} = -R_3 k^2 \Phi_0, \quad \mathrm{D}_I(\mathrm{D}_I - 1)\,\Phi_{-1} = 0.$$

The leading-order equations show that the balance in the cell conservation equation is between diffusion and the up-swimming of the micro-organisms.

The first- and second-order solutions, when the boundary conditions at $z_I = 0$ have been imposed, are

$$W_{-1} = z_I^2(\alpha_{-1}z_I + \beta_{-1}) + k^2R_4(1 + z_I - \exp(z_I)), \quad \Phi_0 = \exp(z_I)$$

and

$$W_{-2} = z_I^2(\alpha_{-2}z_I + \beta_{-2}) + k^2R_3(1 + z_I - \exp(z_I)), \quad \Phi_{-1} = 0,$$

where α_{-1}, β_{-1}, α^{-2} and β_{-2} are constants. When the inner and outer solutions are matched in the usual manner (see e.g. Kevorkian & Cole 1981), it can be shown that there is a non-trivial solution if and only if

$$(A_0 + B_0)\sinh k - kA_0\cosh k = \alpha_{-1} = \alpha_{-2} = \beta_{-1} = 0.$$

The Rayleigh number, R_4, is determined from the solvability condition on the inner system of equations by integrating the cell conservation equation at third order from $z_I = -\infty$ to 0. This gives

$$R_4 = 2/[1-G_{-2}(1+\alpha_0)], \tag{4.43}$$

$$A_0 = -\frac{k^2 R_4 \sinh k}{\sinh^2 k - k^2}, \quad B_0 = -k^2 R_4 (k\cosh k - \sinh k)$$

and

$$\beta_{-2} = k^3 R_4 (\sinh k \cosh k - k)/\sinh^2 k - k^2).$$

Equation (4.43) is valid provided that

$$G_{-2} = d^2 G < (1+\alpha_0)^{-1}, \tag{4.44}$$

and it is reasonable to suppose that if (4.44) does not hold then oscillatory solutions may exist, and an asymptotic analysis based on a scaling in which $\sigma = O(d^2)$ is required. To find the dependence of R on the wavenumber k, the inner solvability condition at fourth order implies that

$$R_3 = 4R_4 \beta_{-2}/k^2,$$

so that

$$R = \frac{2d^4}{1-d^2 G(1+\alpha_0)}\left\{1 + 4d^{-1}\frac{k(\sinh k\cosh k - k)}{\sinh^2 k - k^2} + O(d^{-2})\right\}. \tag{4.45}$$

R_3 is a monotonically increasing function of k and it is readily shown that the above analysis is valid in the limit as k tends to zero. Thus the critical wavenumber predicted by this analysis is zero, provided that (4.44) holds and $k \leqslant O(1)$. However, the numerical solutions of §5 show that for values of G larger than some critical value G_c, the most unstable wavelength is $O(d)$, giving convection cells of a horizontal wavelength commensurate with the sublayer depth l. When $d = 40.0$ and $\alpha_0 = 0$, then $0.7 < d^2 G_c < 0.8$ but the asymptotic analysis does not predict G_c, unlike the shallow-layer case, suggesting that d has to be very large for good agreement.

A calculation similar to that leading to (4.45), using the same inner and outer variables, gives the growth rate $\sigma(R, k)$ when $\sigma = O(1)$, and after some algebra it can be shown that

$$\sigma = k^2\left(\frac{R-R(k)}{R(k)}\right) + O(d^{-1}\delta, d^{-2}), \tag{4.46}$$

where $R(k)$ is the neutral curve given by (4.45). In this case σ is real and so the solution is stationary. Equation (4.46) has been derived from a more complicated transcendental equation by expanding in a Taylor series in powers of

$$\delta = \frac{R-R(k)}{R(k)S_c},$$

which is assumed to be small, given $S_c \approx 20$ in the experiments.

The possible balances between terms in the solvability conditions can be examined to show that the neutral curve is given by an expression of the form of (4.45) wherever G satisfies (4.44). The full leading-order solution (i.e. combining the inner and outer solutions) can be shown to be mode 1.

Returning to the question of oscillatory solutions when $\mathrm{Im}(\sigma) = O(d^2)$, it is straightforward to show that the scaling in (4.42) leads only to the trivial solution unless both $\mathrm{Im}(\sigma) = 0$ and $\sigma \leqslant O(1)$. It appears that terms on the right-hand side of (4.41*b*) are required at leading order to find a non-trivial solution, but such a scaling yields an ordinary differential equation with exponential coefficients which we have been unable to solve analytically.

5. Numerical results

Solutions to the full, linear stability problem (3.11), (3.12) and (3.13), were calculated with a fourth-order accurate, finite-difference scheme provided by Dr D. R. Moore (Cash & Moore 1980). This scheme was used to compute (i) neutral curves in the (R, k)-plane on which $\mathrm{Re}(\sigma) = 0$, and (ii) the growth rate as a function of k for given values of R.

5.1. *Technique*

Initially, values of G, α_0, d and k are supplied, and the values of R and the velocity and cell concentration fields, $W(z)$ and $\Phi(z)$, are estimated, either from analytic results, or from previous numerical results, or by imposing a roughly sinusoidal variation in $\Phi(z)$ and $W(z)$. The scheme is iterated until it converges to a solution, or should it have failed to converge another starting guess is tried. In practice, the numerical solution is most sensitive to the initial guess for R, and relatively independent of the initial W- and Φ-fields. Once a solution, necessarily in a particular mode of disturbance, is established it can be used as the initial guess for neighbouring parameter values, and hence the neutral curve for that particular mode can be determined. Different initial choices of R cause convergence to different modes. Except where the neutral curves for two or more modes become arbitrarily close or cross, they can always be followed provided that the increments in the given parameters are sufficiently small. When modes cross, it is possible to approach along the neutral curves from both sides of the intersection, and often by trial and error to choose the increments in parameters so that the solution jumps across the intersection. The scheme is rendered more efficient by scaling the variables as suggested by the asymptotic analysis of §4, according to whether this layer is shallow, $d \ll 1$, or deep $d \gg 1$. In addition, for the deep layer, the coordinate mesh in the z-direction is stretched by a hyperbolic tangent function to accommodate more points within the exponential boundary layer at the upper surface, than in the outer region below it.

5.2. *Accuracy*

The dependence of the numerical solution on the number and position of the grid points was tested for many different parameter values. Four- to six-figure accuracy was always achieved when the minimum of 21 grid points was used, and the shallow- and deep-layer versions also coincided to this accuracy. Where appropriate, comparisons with the asymptotic values of R from §4 have been shown to agree to within the accuracy of the expansions and further details are given in the results below.

5.3. *Stationary solutions*

Neutral curves when G is zero or small are shown in figure 2 for various values of d, the dimensionless depth of the layer (see (3.2)). In figure 2(*a*), $d = 0.1$ and comparisons are made between the numerical solutions for $R^{(1)}(k)$ and the asymptotic result (4.21) for Case I. Equation (4.21) is valid for values of $k \leqslant O(d)$. When $G = 0$ there is close agreement for values of $k \leqslant 1.0$ and in the limit as $k \to 0$ the numerical solution and asymptotic result agree to 3 significant figures and give $R^{(1)} \to 757$ as $k \to 0$. In the second case, $G = 0.5$ and $\alpha_0 = 0.2$, and again both solutions agree to 3 significant figures as $k \to 0$ to yield $R^{(1)}(0) = 761$. The results begin to diverge significantly when $k \geqslant 0.5$. In addition, the numerical result shows that $R^{(1)}$ has a minimum value of 152 at a critical wavenumber $k_c = 4.4$. This value of $G(=0.5)$, which is sufficient to produce a finite critical wavelength, is small compared with that for a typical suspension of *C. nivalis*, namely $G = 0.5d^{-2} = 50.0$ when $d =$

0.1. By examination of the vertical velocity field, it is possible to show that these solutions are mode 1 solutions. Also, in figure 2(*a*) it can be seen that the suspension is more unstable (i.e. the minimum value of R is smaller) when $G = 0.5$ than when $G = 0$. Comparisons between the numerical solutions and those of (4.45) when $d = 40.0$, $\alpha_0 = 0$ and $d^2G = 0$ and 0.9 are shown in figure 2(*b*). The asymptotic analysis is valid for wavenumbers $k \leqslant O(1)$, and for $G = 0$ it begins to diverge from the numerical solution when $k = 10$. For $d^2G = 0.9$, the solutions diverge significantly when $k > 1$, and $k_c = 16.0$. When $d = 40.0$ and $\alpha_0 = 0$, the critical wavenumber becomes non-zero as d^2G is increased, and the critical value of d^2G lies between 0.7 and 0.8. For larger values of k, the numerical solution shows that $R \sim k^2$ whereas $R \sim k$ in (4.45). When $d = 10$, (4.45) underestimates the computed value of R by about 25% when $k = 1.0$. Such relatively poor agreement in this case is not unexpected because the magnitude of the second term in (4.45) is 80% of that of the first term, so the convergence of the asymptotic expansion is slow.

Neutral curves for the intermediate value of $d = 1.0$, which is not covered by the asymptotic analysis, are shown in figure 2(*c*). Again, when $G = 0$, $R^{(1)}$ has a minimum at $k = 0$ and $R^{(1)}(0) = 1185$. These results imply that, in the absence of gyrotaxis, the critical wavenumber is always zero, which confirms the findings of CLS. Also shown in figure 2(*c*), for completeness, is an example of a higher branch of the neutral curve, $R^{(2)}$, when $G = 0$, and an example of the effects of small values of G, $G = 0.1$. In the latter case, the neutral curve has a minimum $R_c^{(1)} = 858$ at $k_c = 3.5$. This value of G is a fifth of the typical value for *C. nivalis* when $d = 1.0$.

Neutral curves for larger values of G are shown in figure 3, in which we plot $RG(1+\alpha_0)$ versus k, as suggested by (4.36). For $d \leqslant 1$, the critical values of the neutral curves occur at wavenumbers between 4.0 and 5.0 while as d increases from 1.0 to 10.0 both R_c and k_c increase. Along parts of the neutral curves when $d = 1.0$ and $d = 10.0$, indicated by dashed lines in figure 3, the solution corresponding to the branch $R^{(1)}(k)$ is mode 2 not mode 1. As k is decreased below k_c along such a branch, the single convection cell which extends throughout the depth of the layer becomes augmented by a second small convection cell, which forms at the upper boundary at some particular value of k and grows in depth as k is decreased further. Likewise, as k is increased above k_c along such a branch a second small convection cell appears at the bottom of the layer and grows in height as k is still further increased. However, in all such cases examined, with one exception discussed under oscillatory solutions, the solution is of mode 1 within a finite interval containing k_c so that mode 1 is still the most unstable stationary mode. This behaviour is reminiscent of a result of PHK, who found that in an infinitely deep, uniform suspension for which $\alpha_0 > \frac{1}{3}$, modes with a vertical wavenumber greater than zero are the most unstable. However, here there is no 'α_0-cut off', i.e. mode 2 can be found in parts of $R^{(1)}$ even when $\alpha_0 = 0$.

For a further comparison with PHK, we show the effects of changing the boundary conditions to those of stress-free boundaries (for which all instabilities are stationary, as proved in the Appendix). In figure 4, $d = 0.1$, $G = 50$ and $\alpha_0 = 1.0$, and the neutral curves for different modes cross one another, so that although the most unstable mode is mode 1 overall, there are values of k at which mode 2 is the most unstable mode. A second notable feature, which demonstrates the importance of the boundary conditions, is that even at this large value of G, $k_c = 0$. This has been found to be true for all values of G and d investigated. For example when $d = 10$, $G = 10$ and $\alpha_0 = 1$, $R \to 125$ as $k \to 0$.

To complete this section on stationary solutions, we plot the growth-rate curve for the case when $d = 1.0$, $G = 0.5$ and $\alpha_0 = 0.2$, in figure 5. A Rayleigh number a little

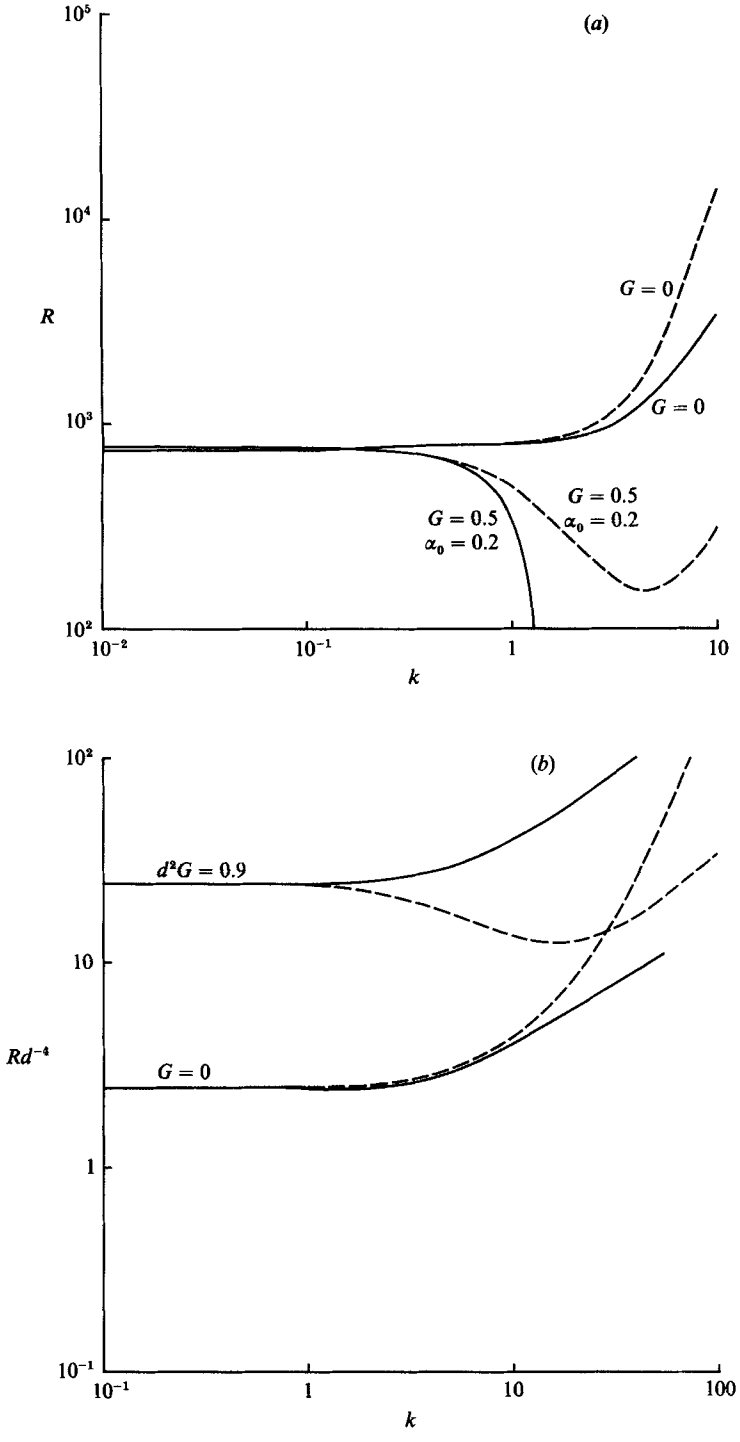

FIGURE 2(*a*, *b*). For caption see facing page.

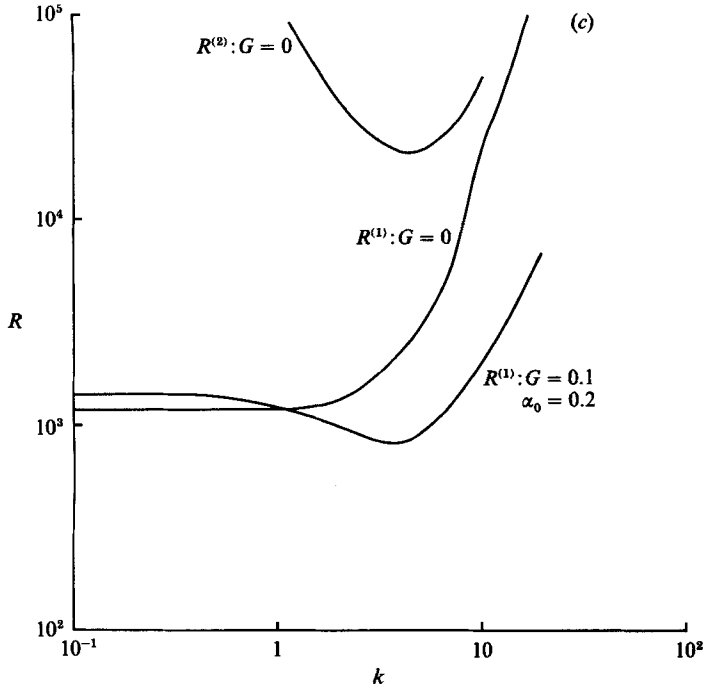

FIGURE 2. (*a*) $d = 0.1$. Comparisons between the numerical results (dashed lines) and neutral curves (solid lines) for the branch $R^{(1)}(k)$ predicted by (4.21). (*b*) Comparison between numerical solutions (dashed lines) and equation (4.45) (solid lines) when $d = 40$ and $d^2G = 0$ and 0.9 for the branch $R^{(1)}(k)$ on the neutral curve. (*c*) Neutral curves for $d = 1.0$.

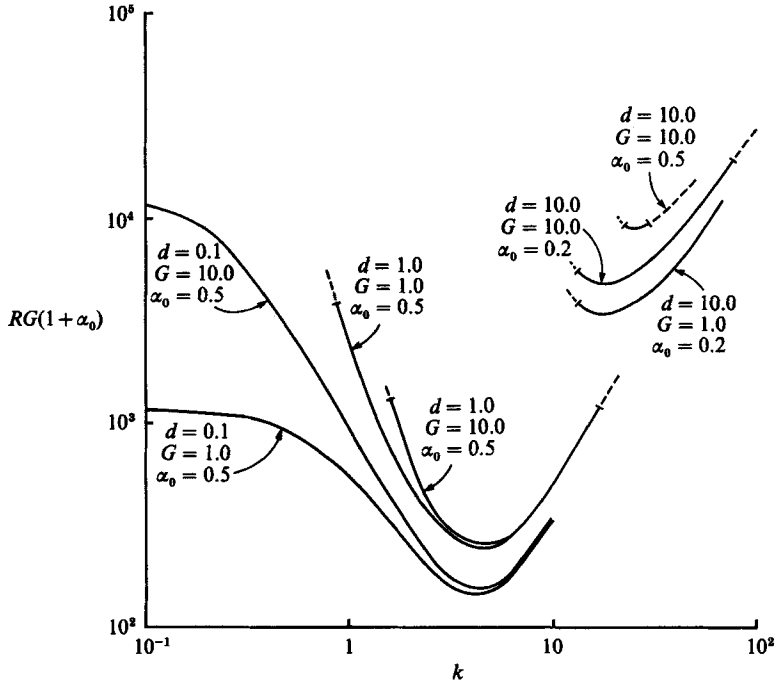

FIGURE 3. Neutral curves on the branch $R^{(1)}(k)$ when $G = 1.0$ and 10.0. The broken lines indicate a change of mode.

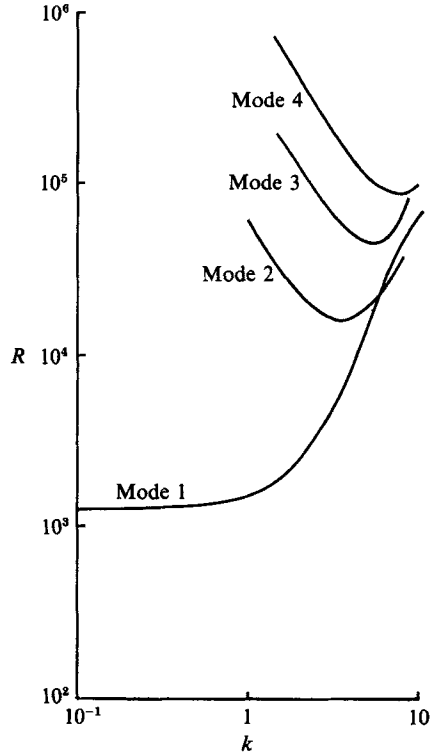

FIGURE 4. Neutral curves when both boundaries are stress-free, showing crossing of neutral curves on different solution branches. Here $d = 0.1$, $G = 50$ and $\alpha_0 = 1$.

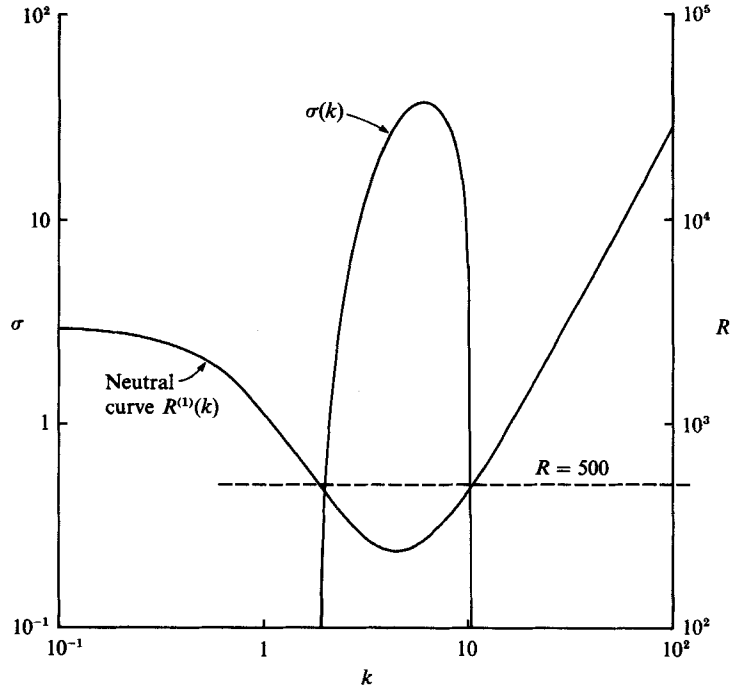

FIGURE 5. Neutral curve $R^{(1)}(k)$ and the growth rate σ at $R = 500$, when $d = 1.0$, $G = 0.5$, $\alpha_0 = 0.2$ and $S_c = 20$. Note that the maximum value of σ occurs at a value of $k > k_c$.

above the minimum of the neutral curve (which is also shown for convenience) was specified and S_c was set to 20. This graph is typical of the growth rate for all parameter values and such plots show that the maximum growth rate is found at wavenumbers $k > k_c$, so that λ_c, which is the estimate of the value of the horizontal pattern spacing when a suspension is just unstable, is likely to overestimate the observed wavelengths.

5.4. *Oscillatory modes*

Overstable, or oscillatory, solutions are found in regions of parameter space not covered by the analysis of §4. The existence of oscillatory solutions explains the failure of the proof of exchange of stabilities in the Appendix. A survey of the relevant parameters for $d = 0.1$, 1.0 and 10.0 has led to the following results.

(i) Oscillatory modes were not found when $d^2G(1+\alpha_0) < 1$, except when α_0 is very close to 1 (see (ii)).

(ii) When $d = 0.1$, $k \geqslant 7.0$ and $\alpha_0 \geqslant 0.97$, overstability is found for all positive values of G examined.

(iii) In general, the most unstable mode was stationary but, when $d = 10.0$, the values of the stationary and oscillatory branches depended on the values of both G and α_0, and there were values of G and α_0 for which the most unstable mode was oscillatory.

Neutral curves for two cases when $d = 1.0$ and $d = 10.0$ are shown in figures 6 and 7 and serve to illustrate the general behaviour. In figure 6, $d = 1.0$ and $\alpha_0 = 1$ and two oscillatory branches bifurcate from the stationary branch at points A and B, to the left and right of the critical point (k_c, R_c) respectively. Here the stationary solution is the most unstable.

The stationary branch consists of a closed loop, the lower half of which can be shown to be smoothly connected to the branch $R^{(1)}(k)$ as G and α_0 are varied until $d^2G(1+\alpha_0) < 1$ and there are no oscillatory branches. Similarly, the upper stationary branch is smoothly connected to $R^{(2)}(k)$. The survey of oscillatory modes indicates that this is the typical behaviour. This particular example is unusual in that, at the critical point $(k_c, R_c) = (3.889, 273.6)$, the solution is mode 2 not mode 1. Examination of the $W(z)$-field shows this solution to consist of one main convection cell with a subsidiary cell in the top 5% of the layer, the maximum vertical velocity of which is less than 0.1% of the maximum in the main cell. Nevertheless, this does represent the only case that has been found in which the most unstable mode is not mode 1. In practice, however, such a mode is unlikely to be seen because it appears to be a limiting case as $\alpha_0 \to 1$, for mode 1 is the most unstable mode when $\alpha_0 = 0.95$.

In figure 7, when $d = 10.0$ and $\alpha_0 = 0.5$, the left-hand oscillatory branch has developed a minimum which is lower than that of the local minimum of the stationary branch, and so (k_c, R_c) lies on the oscillatory branch. The values of d^2G, α_0 and $\omega = \mathrm{Im}\,(\sigma)$ at the critical point are 1.0, 0.5 and 32.1, respectively. d^2G and α_0 are greater than the estimated values for *C. nivalis* (see table 2), for which $d^2G(1+\alpha_0) < 1$ always, and so overstability is not predicted for this species. Nevertheless, $d^2G = 1$ and $\alpha_0 = 0.5$ are within the likely bounds for some micro-organisms and so it may be possible to observe overstability in some future experiment. The period for overstability is 97.7 s. The value of ω is typical of those found when $d = 10.0$, which suggests that σ should be found in the leading-order terms of the asymptotic analysis for the deep layer, although as discussed in §4.2 attempts at a suitable scaling to achieve such a balance have been unsuccessful.

We conclude this topic with an explanation of the mechanism for overstability. As

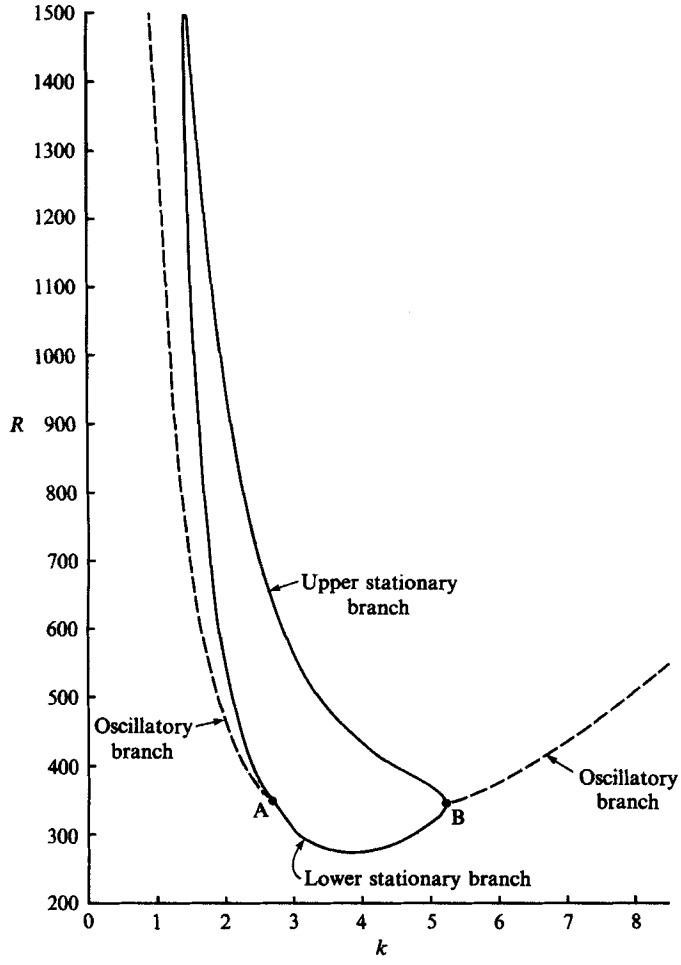

FIGURE 6. Neutral curve $R^{(1)}(k)$ for mode 1 showing both stationary (solid lines) and oscillatory branches (dashed lines). $d = 1.0$, $G = 1.0$, $\alpha_0 = 1.0$ and $S_c = 20$.

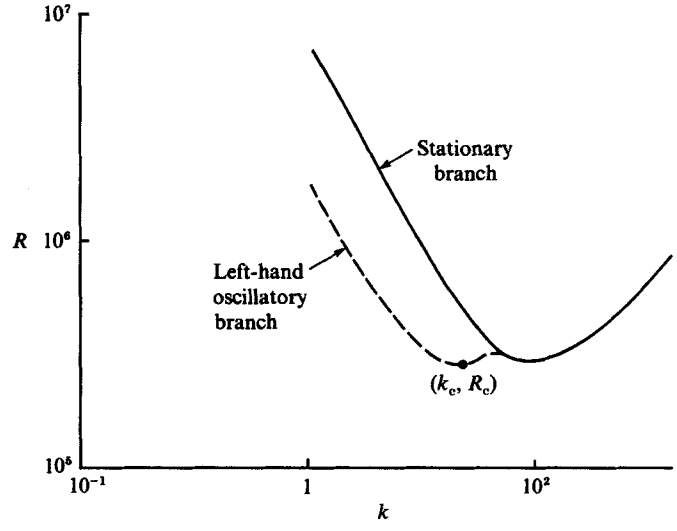

FIGURE 7. Stationary (solid line) and oscillatory branches (dashed line) of $R^{(1)}(k)$ when $d = 10.0$, $d^2G = 1.0$, $\alpha_0 = 0.5$ and $S_c = 20$, showing that the most unstable mode is oscillatory.

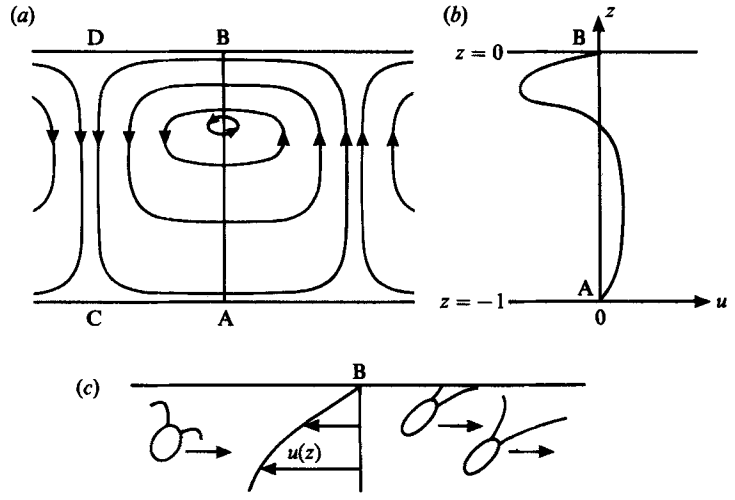

FIGURE 8. Diagrams to illustrate the mechanism for overstability: (*a*) streamlines for a typical convection cell; (*b*) the horizontal velocity profile along AB; and (*c*) close-up of the shear layer near the top boundary, showing the drift of micro-organisms away from the downwelling region towards the upwelling region. (See text for details.)

mentioned in §3, the existence of oscillatory modes is surprising in a system that appears to have only one instability mechanism. On closer inspection, however, there are in fact two instability mechanisms, namely the effect of negative geotaxis (pure 'up-swimming') which leads to a Rayleigh–Taylor instability of heavy fluid over light fluid, as described by CLS, and the purely 'gyrotactic' instability of PHK, which grows from a uniform basic state. However, these two mechanisms seem to cooperate with each other, rather than to compete, and we know that for the case of stress-free top and bottom boundaries this instability is always stationary. Thus there must be yet a third mechanism involving the no-slip condition coupled with gyrotaxis.

Consider the situation depicted in figure 8. There is a single layer of convection cells between the top and bottom boundaries in (*a*), with a horizontal velocity profile which vanishes at the top and bottom boundaries as shown in (*b*). There is a shear layer at each boundary due to the no-slip condition at the rigid boundaries. The 'close-up' in (*c*) of the shear layer near B shows that there is a net viscous torque on the micro-organisms near B so that they swim at an angle to the vertical from left to right, away from the downwelling region along CD, where there is a higher concentration of micro-organisms which drives the bulk convection. At the bottom near A, the flux of cells is always away from the downwelling region, as is the case when the bottom boundary is stress-free. The layer close to the upper boundary supplies cells to the downwelling region, so if the parameter values are such that the drift of micro-organisms in the top layer is sufficiently great that overall there is a net flux of cells away from CD, then the majority of the micro-organisms will move towards the upwelling region until they cause a reversal in the sense of the bioconvection cell and oscillations will ensue.

In support of this argument, we show in figure 9 the horizontal flux of swimming cells and the bulk horizontal velocity and shear profiles when (*a*) $d = 0.1$, $d^2G = 1.0$, $\alpha_0 = 1.0$ and $k = 3.0$ and (*b*) $d = 10.0$, $d^2G = 1.0$, $\alpha_0 = 0.5$ and $k = 4.0$, at the time of maximum convection, assuming that the horizontal planform consists of rolls. The profiles are measured through the centre of the convection cells, i.e. along lines like

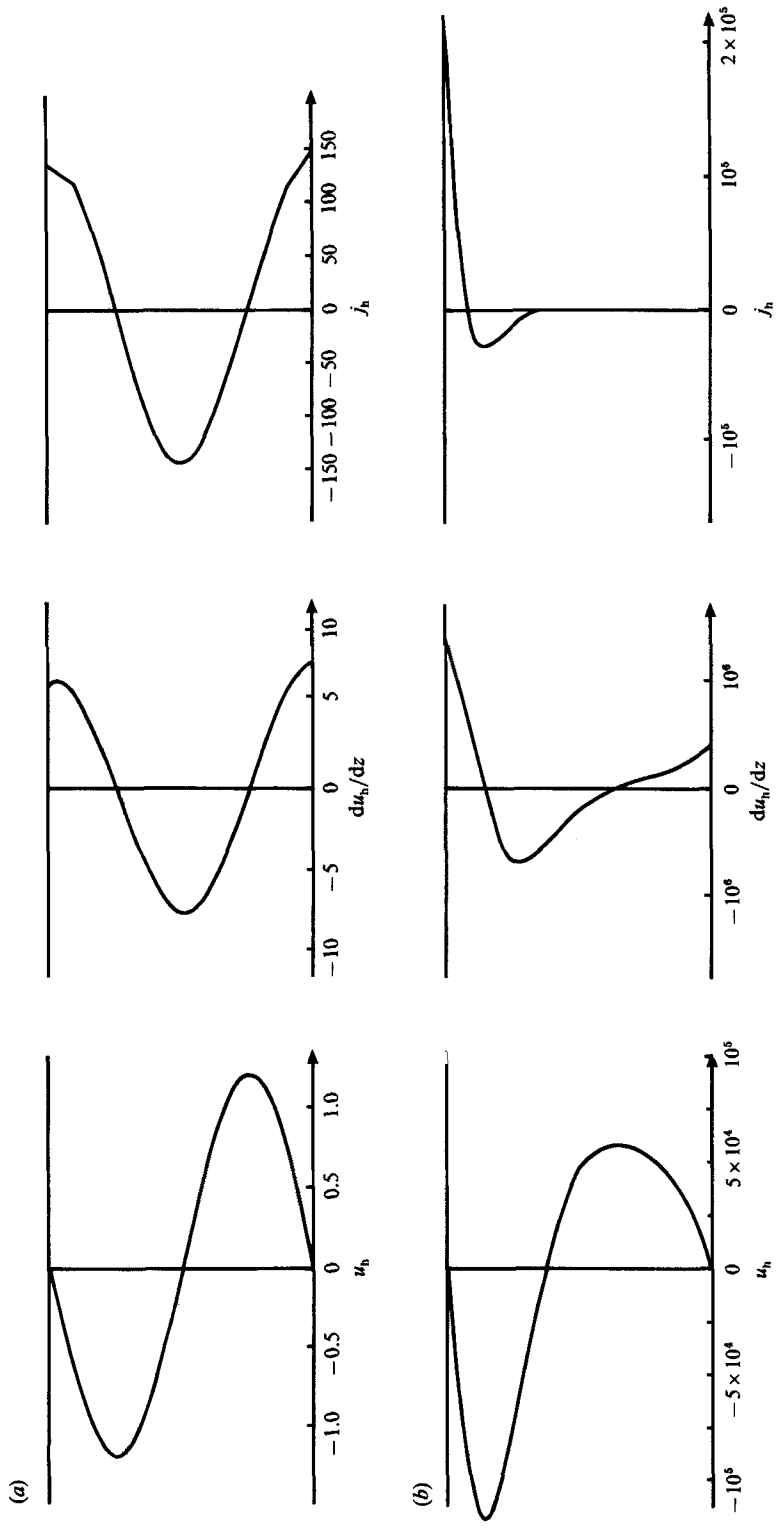

FIGURE 9. Graphs of the horizontal velocity $u_h(z)$, horizontal shear du_h/dz and the horizontal component of the flux of swimming micro-organisms $j_h(z)$ in dimensionless units for the two cases: (*a*) $d = 0.1$, $d^2G = 1.0$, $\alpha_0 = 1.0$ and $k = 3.0$; (*b*) $d = 10.0$, $d^2G = 1.0$, $\alpha_0 = 0.5$ and $k = 4.0$.

(*a*)	α_0	k_c (dimensionless)	λ_c^* (cm)	R_c
	0	0.81	7.8	0.97×10^6
	0.2	2.1	2.9	1.20×10^6
	0.4	3.3	1.9	1.52×10^6
	0.6	4.5	1.4	1.95×10^6
	0.8	5.9	1.1	2.53×10^6
	1.0	7.3	0.86	3.30×10^6
(*b*)	d^2G	k_c (dimensionless)	λ_c^* (cm)	R_c
	0	0	—	0.49×10^6
	0.25	0	—	0.70×10^6
	0.50	2.1	2.9	1.20×10^6
	0.75	7.1	0.88	2.19×10^6

TABLE 3. The dependence of the most unstable wavelength on G and α_0 for a layer 1.0 cm deep ($d = 20$): (*a*) $d^2G = 0.5$, (*b*) $\alpha_0 = 0.2$

AB in figure 8. In both cases there is overstability and there is a net flux of cells away from the downwelling region. In both cases, the flux is strongly influenced by the horizontal shear.

It is interesting to note that Childress & Peyret (1976) found some evidence of nonlinear oscillations in a numerical study of two-dimensional bioconvection. In their model, the particles executed a random walk together with a drift vertically upwards, so that there was no gyrotaxis.

To complete this section, results on how the critical wavenumber and wavelength vary with α_0 and G are presented in table 3. These apply to the case when $d = 20$, corresponding to a layer depth of 1 cm for the parameter values of a typical suspension of *C. nivalis*, as given in table 2. The results are used in §6 in the discussion of experimental results for such a layer. We see that λ_c^* varies from 7.8 cm to 0.86 cm as α_0 varies from 0 to 1 when $d^2G = 0.5$, our best estimate for G (see table 2). However, G is hard to measure and there is considerable uncertainty about the actual values, as well as the distribution of those values over the population. Table 3(*b*) shows that λ_c^* is sensitive to the value of G. If the error in the estimate of $d^2G = 0.5$ is as much as 50%, then λ_c^* varies between 0.88 cm and ∞. This has to be borne in mind when making comparisons with experiments.

The results of §§4 and 5 may be briefly summarized as follows.

(i) When G is increased from zero, with d and α_0 fixed, the wavelength of the predicted pattern spacing decreases to a finite value which is proportional to the depth H of the layer, and the critical Rayleigh number R_c is lowered. For large values of G, oscillatory solutions are found.

(ii) When d is increased from small values, and G and α_0 are held fixed, R_c is initially lowered but for values of d larger than one, R_c scales like d^4. The pattern wavelength decreases slightly as d increases, but remains roughly proportional to the layer depth H.

(iii) When α_0 is increased, with d and G fixed ($G \neq 0$), R_c is lowered and, at values of α_0 close to one, oscillatory solutions exist.

6. Discussion

The mathematical developments presented here ought to be accompanied by a set of reasonably accurate, experimentally determined parameters which could be used to validate the theory. Unfortunately only estimates are currently available. An

attempt is underway to measure B and D using a focusing apparatus similar to that described in Kessler (1986). Furthermore, direct microscopic measurements (with D.-P. Häder) of algal cell velocity distribution functions will yield better estimates of V_c and possibly D. In this discussion, we first describe some qualitative observations and compare them with the results of this paper and of PHK. It turns out that these particular observations are not sufficiently refined to say which of the two theories best describes the observations, since both agree moderately well, but the exercise does illustrate the necessary analysis. Later in this section, we shall also show that the equilibrium state is more unstable than the uniform suspension when the layer is sufficiently shallow, so that the instability mechanism of this paper should conform with experiments on shallow layers.

A suspension of the alga *C. nivalis*, 1.0 cm deep with a mean concentration of approximately 5×10^5 cells cm^{-3}, was thoroughly mixed by gently swirling the fluid in its container, and then the container was put down on a bench. After about 60 s, patterns were seen as the experiment was being viewed from above. These initial patterns were rectilinear and similar, but less regular, in appearance to those in figures 10, 11 and 12 of Kessler (1985). The initial spacing of concentrated bands of cells was 2–3 cm. It is this very first, visual indication of bioconvection that we shall compare with the results of the linear stability analyses, with the implicit assumption that the typical lengthscales had not yet been grossly modified by nonlinear effects. The patterns continued to develop until they reached a final state in which the spacing was regular, with a value between 0.5 and 1.0 cm. In this final, inevitably nonlinear, state the patterns appear to be steady, but time-lapse photography reveals that they are in fact constantly shifting, on timescales of the order of 10 min. It should also be mentioned that even though bioconvection patterns exhibiting distinct growth rates and wavelengths are unambiguously present, they vary diurnally owing to variations in cell behaviour during their growth cycle. Such behaviour can be induced or enhanced by tilting the suspension or providing non-uniform illumination. It is anticipated that once a few cases are properly measured and integrated into our theory, the understanding derived will help to elucidate mean behaviour changes during the cell cycle.

In order to apply the theory, we need first to decide whether sufficient time had elapsed, before the patterns were first seen, (*a*) for the fluid motions remaining after the mixing to have decayed away, then (*b*) for the equilibrium profile to have been established, and lastly (*c*) for initial perturbations to have developed. A similar discussion was given by PHK. They estimated the decay times for turbulent eddies as H/U, where H is the depth and U a typical stirring velocity. Alternatively, we could suppose that the fluid and container are in solid-body rotation with angular velocity $\boldsymbol{\Omega}$, and at $t = 0$ the container is brought to rest. The timescale for spin-down of the fluid by the Ekman boundary layers is $O(E^{-\frac{1}{2}}\Omega^{-1})$, where $E = \nu/\Omega H^2$ is the Ekman number; the timescale for decay of the residual motions is also $O(E^{-\frac{1}{2}}\Omega^{-1})$ (Greenspan 1968). If $\Omega = 1$ s^{-1}, the resulting decay time is $O(E^{-\frac{1}{2}}) \approx 10$ s, larger than H/U when $U > (\Omega\nu)^{\frac{1}{2}} = 0.1$ cm s^{-1}.

Using the estimates in table 2 for the parameter values for a suspension of *C. nivalis*, the time for development of the exponential concentration profile is of the order of the time taken for a typical algal cell to swim from the bottom to the top of the layer, which is about 100 s since $H = 1$ cm (PHK).

Turning to the instability of the equilibrium state, we note first that the values of k_c and R_c depend on α_0 and G as shown in table 3. Our best estimates for α_0 and d^2G are 0.2 and 0.5, respectively, and for a layer of depth $H = 1$ cm, we find that the

$\bar{n}$ (cells cm^{-3})	R	k_{max}	λ^*_{max} (cm)	σ_{max}	t^*_g (s)
6.015×10^5	1.203×10^6	2.18	2.88	4.16×10^{-3}	4.81×10^5
6.080×10^5	1.216×10^6	2.52	2.49	7.12×10^{-3}	2.81×10^5
6.400×10^5	1.280×10^6	3.36	1.87	6.39×10^{-1}	3.13×10^3
8.000×10^5	1.600×10^6	5.36	1.17	7.70×10	30.0
1.200×10^6	2.400×10^6	8.02	0.78	5.05×10^2	3.96

TABLE 4. Timescale for the growth of perturbations from the equilibrium solution. Here $\alpha_0 = 0.2$, $S_c = 20$, $H = 1$ cm, $d^2G = 0.5$, $D = 5 \times 10^{-4}$ cm^2 s^{-1} and $R_c = 1.20 \times 10^6$ corresponding to a mean cell concentration $\bar{n}_c = 6.0 \times 10^5$ cells cm^{-3}.

(dimensionless) critical wavenumber $k_c = 2.1$, corresponding to a pattern wavelength of 2.9 cm, in good agreement with the observations of early pattern spacing. The mean concentration of cells $\bar{n}$ is related to R by (2.16) and (3.16); using the parameter values in table 2 for a suspension of *C. nivalis* and setting $H = 1$ cm gives $R = R_c$ when $\bar{n} = \bar{n}_c \equiv 6.0 \times 10^5$ cells cm^{-3}. Again this agrees well with the mean concentration in the experiment.

The timescale t^*_g for the growth of perturbations can also be calculated and compared with the experiment. In table 4 are given the maximum growth rate σ_{max} and corresponding wavelength λ^*_{max} as a function of $\bar{n}$ (and R) when $\alpha_0 = 0.2$, $d^2G = 0.5$ and $H = 1$ cm. $t^*_g = H^2/D\sigma_{max}$ is also given. When $\bar{n} = 6.015 \times 10^5$ cells cm^{-3}, which is just greater than $\bar{n}_c$ so that the suspension is slightly unstable, $t^*_g = 4.81 \times 10^5$ s which is far in excess of the observed timescale. With a larger $\bar{n}$ of 8×10^5 cells cm^{-3}, $t^*_g = 30$ s but $\lambda^*_{max} = 1.17$ cm, which is smaller than the observed pattern spacing. Moreover, when allowance is made for the time taken for the development of the equilibrium state, t^*_g can only be a few seconds long. To achieve this requires a concentration significantly larger than that actually present; for example $t^*_g = 3.96$ s when $\bar{n} = 1.2 \times 10^6$ cells cm^{-3}, and then the predicted value of λ^*_{max} is smaller still: $\lambda^*_{max} = 0.78$ cm. Although we are comparing the theory only with qualitative results, neither of the last values of $\bar{n}$ and λ^*_{max} agrees well with this particular experiment. Of course, t^*_g is sensitive to the chosen value of the diffusion coefficient D, and a generous error in its value gives $D = 5 \times 10^{-3}$ cm^{-3} cm^2 s^{-1} (Kessler 1986). In this case, $t^*_g = 3.0$ s when $\lambda^*_{max} = 1.7$ cm, but $\bar{n}$ increases like D^2 giving a corresponding mean cell concentration of 8×10^7 cell cm^{-3}, which is manifestly too great. We conclude that any increase in the assumed value of D worsens the agreement with experiment.

If instead we consider PHK's instability mechanism and use the parameter values in table 2, we find that when $H = 1$ cm the suspension is just unstable if $\bar{n} = 1.2 \times 10^6$ cells cm^{-3} and, correspondingly, $t^*_g = 25$ s and $\lambda^*_{max} = 1.7$ cm. This value of λ is reasonably close to the experimental one, and the timescale for the decay of fluid motions plus t^*_g are consistent with the time taken for the pattern first to appear. Thus in this particular experiment it seems likely that once the fluid motions arising from the mixing had decayed sufficiently, the suspension was approximately uniform, with a sufficiently large mean cell-concentration that it was immediately unstable to small perturbations. However, if $\bar{n}$ was less than 1.2×10^6 cells cm^{-3}, the uniform state would have been stable and the mechanism of this paper better describes the instability. Confirmation of these arguments must await more quantitative experiments.

Further insight into the interpretation of the theories of this paper and of PHK can be gained by comparing the neutral stability curves for the two states for layers

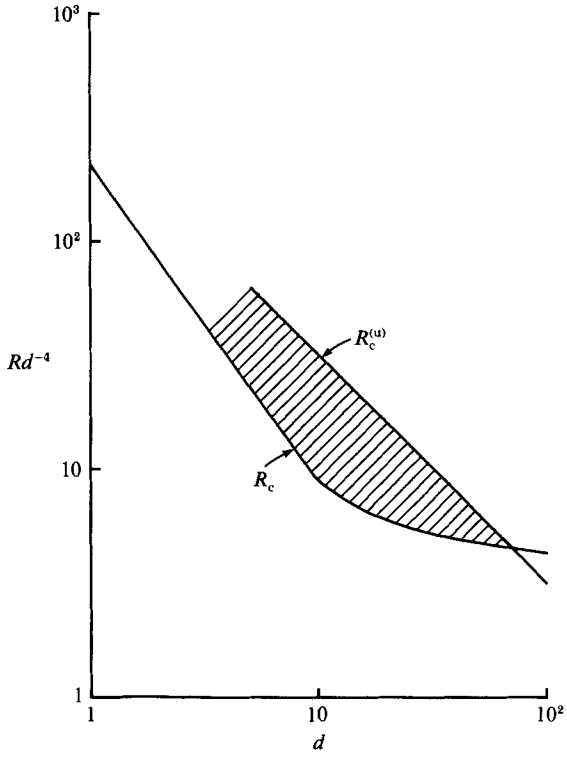

FIGURE 10. Critical Rayleigh numbers R_c and $R_c^{(u)}$ versus scaled depth d for instabilities of the equilibrium and uniform states respectively. Here $d^2G = 0.5$ and $\alpha_0 = 0$.

of different depths. For convenience, we consider only spherical micro-organisms, for which $\alpha_0 = 0$, and take

$$G = 0.5d^{-2},$$

which is a typical value for *C. nivalis*. PHK estimate the critical Rayleigh number, $R_c^{(u)}$, for the uniform suspension to be

$$R_c^{(u)} = 16\pi^2 V_c/DG(1-\exp(-d))$$

(in the notation of this paper), where the exponential term arises from the relationship (2.16) between N and $\bar{n}$. In figure 10, we plot $R_c^{(u)}$ as a function of d together with numerical values of the R_c for the equilibrium profile. From this graph we conclude, for a given layer depth H, that

(i) the suspension is stable whenever R is less than the values on both curves;

(ii) the suspension is unstable when R is greater than the values on both curves;

(iii) when R lies in the shaded region between the two curves; the suspension is unstable if it is in the equilibrium state, but not if it is uniform; and

(iv) the curves cross at $d \approx 70$.

Suppose that we carry out an experiment in which the Rayleigh number lies in the shaded region. Then, as the residual fluid motions from the mixing decay, the suspension is initially almost uniform and, because $R < R_c^{(u)}$, it is stable, so the cells begin to swim upwards to form the exponential concentration profile of the equilibrium state. However, the equilibrium state is unstable ($R > R_c$) so that during the formation of the exponential concentration profile the suspension becomes unstable at a state in between the uniform and equilibrium states. So, if

$R_c < R < R_c^{(u)}$, we shall observe that the cells will begin to form a dense upper layer in the suspension which spontaneously begins to convect, before the equilibrium state has fully developed. The two curves in figure 10 cross at $d \approx 70$, i.e. $H \approx 3.5$ cm for a suspension of *C. nivalis*, so that if bioconvection patterns form at all in layers deeper than about 3.5 cm, they will do so only from a more or less uniform suspension and gyrotaxis is the sole instability mechanism.

This conclusion is consistent with observation. For typical suspensions of *C. nivalis*, in layers less than a centimetre or two deep, bioconvection patterns appear and grow from the upper regions of the suspension, but in deeper layers plumes form spontaneously in the interior regions. This behaviour persists into the fully developed, nonlinear regime: in shallow layers bioconvection patterns extending throughout the entire depth of the layer can be seen, whereas in deep layers most of the patterns consist of regularly spaced plumes standing on the bottom boundary and extending only into the middle of the layer. In the absence of gyrotaxis, Harashima *et al.*'s (1988) numerical solution showed that the plumes originate near the top of the layer for the two depths $H = 2$ cm and 5 cm which they considered.

A mathematical description of the nonlinear, bottom-standing plumes is one target for future research. Another topic for future consideration is the prediction of the initial planform of the bioconvection patterns using weakly nonlinear theory. It is also observed that initial patterns take the form of rolls bounded on one side by falling curtains of dense fluid, which in turn break up into plumes. This indicates that the initial two-dimensional disturbance has become unstable to a three-dimensional mode. An important feature which has to be included in the continuum model is that the suspension consists of a varied population of micro-organisms, and in particular the diffusion tensor D should be derived from a statistical description of the individual dynamics averaged over the population. A potential large-scale consequence of such a description is a better understanding of the patchiness of algal populations in nature, for example with reference to red tides. Quantitative experimental studies are needed both to test the current theory and to provide better estimates of the values of the parameters that characterize suspensions of different micro-organisms. Lastly, a potentially rich area for investigation with applications in the study of dynamical systems is a study of the effects of competing external influences, such as changes in lighting, on bioconvection and the subtle reorganization of the patterns which takes place over minutes or hours.

We should like to thank Dr D. R. Moore for supplying the finite-difference scheme for solving the two-point boundary-value problem. Financial support from the Science and Engineering Research Council and the National Science Foundation (Grant no. INT 85-13696) is gratefully acknowledged.

Appendix. Conditions for the absence of oscillatory modes

In this Appendix, we prove that on a neutral curve where $\mathrm{Re}\,(\sigma) = 0$, then $\mathrm{Im}\,(\sigma) = 0$ also for solutions of (3.11) and (3.12) subject to the boundary conditions (3.13) and (3.14) for stress-free boundaries.

Suppose that on the neutral curve $\sigma = \mathrm{i}\omega$, where ω is real. Equation (3.11) is multiplied by $\overline{W}(z)$, the overbar denoting the complex conjugate, and integrated from $z = -1$ to 0. Integrating by parts and applying the boundary conditions yields

$$\int_{-1}^{0} \{|W''|^2 + (2k^2 + \mathrm{i}\omega S_c^{-1})|W'|^2 + k^2(k^2 + \mathrm{i}\omega S_c^{-1})|W|^2 + k^2 R d^{-1} \overline{W}\Phi\}\,\mathrm{d}z = 0, \quad \text{(A 1)}$$

where primes indicate derivatives with respect to z. Similarly when (3.11) is multiplied by $\overline{W}''(z)$ and integrated we find that

$$-[\overline{W}''W''']_{-1}^{0}+\int_{-1}^{0}\{|W'''|^2+(2k^2+\mathrm{i}\omega S_c^{-1})|W''|^2 + k^2(k^2+\mathrm{i}\omega S_c^{-1})|W'|^2-k^2Rd^{-1}\overline{W}''\Phi\}\,\mathrm{d}z=0. \tag{A 2}$$

The integrated term in (A 2) vanishes only at a free boundary where $W''(z)=0$. The complex conjugate of (3.12) for the conservation of cells is multiplied by $\exp(-dz)\,\Phi(z)$ and integrated from $z=-1$ to $z=0$, which gives

$$[d\exp(-dz)|\Phi'|^2]_{-1}^{0}-\int_{-1}^{0}\{\exp(-dz)((k^2-\mathrm{i}\omega)|\Phi|^2+|\Phi'|^2) -dG(1+\alpha_0)\,\overline{W}''\Phi+d(G(1-\alpha_0)+1)\,\overline{W}\Phi\}\,\mathrm{d}z=0. \tag{A 3}$$

Finally (A 1) is multiplied by $d[G(1-\alpha_0)+1]$, (A 2) is multiplied by $d[G(1+\alpha_0)]$ and their sum is added to k^2Rd^{-1} times (A 3). On taking the imaginary part, we find that

$$\omega S_c^{-1}\int_{-1}^{0}\{dG(1+\alpha_0)(|W''|^2+k^2|W'|^2)+d(G(1-\alpha_0)+1)(|W'|^2+k^2|W|^2) +S_c\,k^2Rd^{-1}\exp(-dz)|\Phi|^2\}\,\mathrm{d}z=dG(1+\alpha_0)\,\mathrm{Im}([\overline{W}''W''']_{-1}^{0}). \tag{A 4}$$

There is no contribution to (A 4) from the integrated term in (A 3) which is real, but the integrated term in (A 2) forms the right-hand side of this last result. The right-hand side vanishes in the case of two free boundaries, which implies that $\omega=0$, proving exchange of stabilities in this case. In fact, this result is true even if $\mathrm{Re}(\sigma)\neq 0$.

REFERENCES

Cash, J. R. & Moore, D. R. 1980 A high order method for the numerical solution of two-point boundary value problems. *BIT* **20**, 44–52.

Chandrasekhar, S. 1961 *Hydrodynamic and Hydromagnetic Stability*. Oxford University Press.

Childress, S., Levandowsky, M. & Spiegel, E. A. 1975 Pattern formation in a suspension of swimming micro-organisms: equations and stability theory. *J. Fluid Mech.* **63**, 591–613 (referred to as CLS).

Childress, S. & Peyret, R. 1976 A numerical study of two-dimensional convection by motile particles. *J. Méc.* **15**, 753–779.

Drazin, P. G. & Reid, W. H. 1981 *Hydrodynamic Stability*. Cambridge University Press.

Greenspan, H. P. 1968 *The Theory of Rotating Fluids*. Cambridge University Press.

Harashima, A., Watanabe, M. & Fujishiro, I. 1988 Evolution of bioconvection patterns in a culture of mobile flagellates. *Phys. Fluids* **31**, 764–775.

Hurle, D. T. J., Jakeman, E. & Pike, E. R. 1967 On the solution of the Bénard problem with boundaries of finite conductivity. *Proc. R. Soc. Lond.* A**296**, 469–475.

Ince, E. L. 1956 *Ordinary Differential Equations*. Dover.

Jeffrey, G. B. 1922 The motion of ellipsoidal particles immersed in a viscous fluid. *Proc. R. Soc. Lond.* A**102**, 161–179.

Kessler, J. O. 1984 Gyrotactic buoyant convection and spontaneous pattern formation in algal cell cultures. In *Nonequilibrium Cooperative Phenomena in Physics and Related Fields* (ed. M. G. Velande), pp. 241–248. Plenum.

Kessler, J. O. 1985 Cooperative and concentrative phenomena of swimming micro-organisms. *Contempt. Phys.* **26**, 147–166.

Kessler, J. O. 1986 Individual and collective fluid dynamics of swimming cells. *J. Fluid Mech.* **173**, 191–205.

KEVORKIAN, J. & COLE, J. D. 1981 *Perturbation Methods in Applied Mathematics.* Springer.

PEDLEY, T. J., HILL, N. A. & KESSLER, J. O. 1988 The growth of bioconvection patterns in a uniform suspension of gyrotactic micro-organisms. *J. Fluid Mech.* **195**, 223–238 (referred to as PHK).

PEDLEY, T. J. & KESSLER, J. O. 1987 The orientation of spheroidal microorganisms swimming in a flow field. *Proc. R. Soc. Lond* B**231**, 47–70.